HHS Public Access

Author manuscript

Cell Rep. Author manuscript; available in PMC 2023 October 23.

Published in final edited form as:

Cell Rep. 2023 September 26; 42(9): 113037. doi:10.1016/j.celrep.2023.113037.

Single-nucleus RNA sequencing of developing superior colliculus identifies neuronal diversity and candidate mediators of circuit assembly

James S. Choi[1,3], **Ana C. Ayupe**[1,3], **Felipe Beckedorff**[2], **Paola Catanuto**[1], **Robyn McCartan**[1], **Konstantin Levay**[1], **Kevin K. Park**[1,4,*]

[1]Department of Neurological Surgery, The Miami Project to Cure Paralysis, University of Miami Miller School of Medicine, 1095 NW 14th Ter., Miami, FL 33136, USA

[2]Department of Human Genetics, Sylvester Comprehensive Cancer Center, University of Miami Miller School of Medicine, 1501 NW 10th Avenue, Miami, FL 33136, USA

[3]These authors contributed equally

[4]Lead contact

SUMMARY

The superior colliculus (SC) is a sensorimotor structure in the midbrain that integrates input from multiple sensory modalities to initiate motor commands. It undergoes well-characterized steps of circuit assembly during development, rendering the mouse SC a popular model to study establishment of neural connectivity. Here we perform single-nucleus RNA-sequencing analysis of the mouse SC isolated at various developmental time points. Our study provides a transcriptomic landscape of the cell types that comprise the SC across murine development with particular emphasis on neuronal heterogeneity. We report a repertoire of genes differentially expressed across the different postnatal ages, many of which are known to regulate axon guidance and synapse formation. Using these data, we find that Pax7 expression is restricted to a subset of GABAergic neurons. Our data provide a valuable resource for interrogating the mechanisms of circuit development and identifying markers for manipulating specific SC neuronal populations and circuits.

Graphical abstract

*Correspondence: kpark@miami.edu.

AUTHOR CONTRIBUTIONS

A.C.A., J.S.C., and K.K.P. designed the experiments, conducted the experiments, and wrote the paper. R.M., P.C., and K.L. assisted with the experiment. F.B. contributed to data analysis.

SUPPLEMENTAL INFORMATION

Supplemental information can be found online at https://doi.org/10.1016/j.celrep.2023.113037.

DECLARATION OF INTERESTS

The authors declare no competing interests.

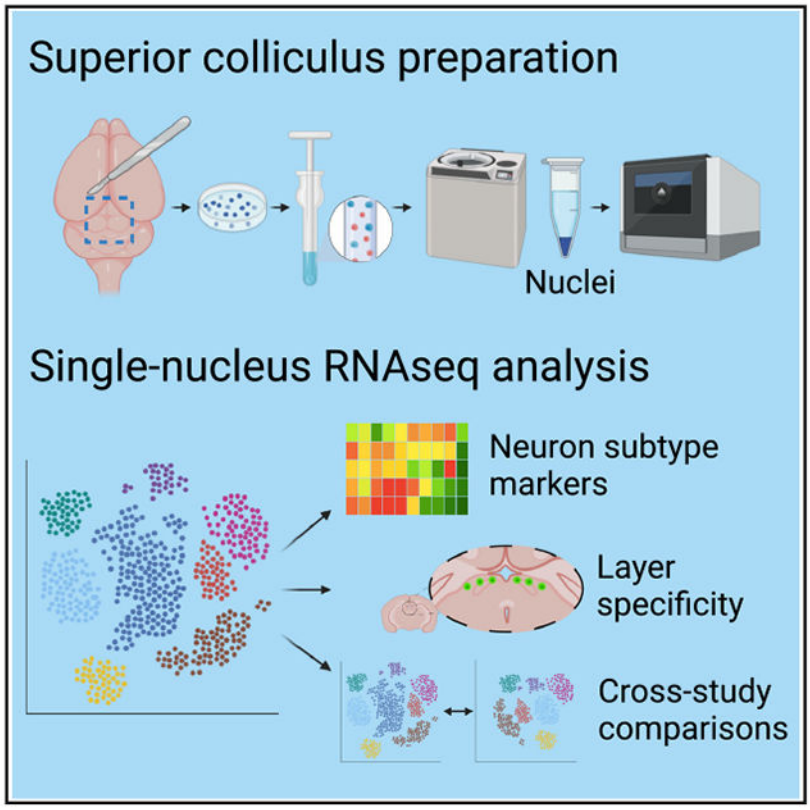

In brief

Choi et al. perform single-nucleus RNA-seq on mouse superior colliculus (SC) at various ages. Results show cell populations and their transcriptional signatures in developing and mature SC. To facilitate open exploration, the authors create a web portal for analyzing SC gene expression profiles across the ages.

INTRODUCTION

The superior colliculus (SC) is a paired sensorimotor structure in the midbrain that receives input from multiple sensory modalities and incorporates environmental stimuli to control innate behaviors. In the mouse, these behaviors include coordinating gaze shifts involving both eye and head movements,[1] escaping or freezing in response to a looming object,[2,3] hunting and approaching responses,[4] and light-/dark-induced sleep and wakefulness.[5]

The SC can be divided into the superficial visuosensory and the deeper motor layers with each subdivision organized into several fibrous and cellular laminae.[6–10] The superficial region consists of the stratum griseum superficiale (SGS) and the stratum opticum (SO) and receives innervation from retinal ganglion cells (RGCs) and the primary visual cortex. Cells in the deeper layer express sensitivity to sensory stimuli from multiple modalities (e.g., vision, audition, and somatosensation) and translate sensory signals into motor commands used to guide orienting movements. Primary outputs from the superficial region include projections to the pulvinar and lateral intermediate areas of the thalamus, which

project to areas of the cerebral cortex that are involved in controlling eye movements. The projections from the deeper layers have also been characterized extensively, which include two descending projections traveling to the brainstem and spinal cord and ascending projections to multiple sensory and motor centers.[8] Given its capacity to register multiple sensory modalities and to coordinate signals into motor commands, the SC has been widely used to investigate the principles underlying both multisensory and sensorimotor processing.

During nervous system development, axon guidance and targeting selection are critical steps toward establishing proper neural circuits. The SC has been a prominent model for investigating the mechanisms by which axons innervate their target regions. Accordingly, studies have revealed that, within each SC lamina, RGC inputs are mapped topographically with respect to the visual field; the temporal-nasal axis of the retina projects along the anterior-posterior axis of the SC, and the dorsal-ventral axis of the retina projects along the lateral-medial axis of the SC. The formation of topography along these axes results from molecular labels such as Eph receptors and ephrin.[11–14] Others have used transgenic mice to demonstrate that different RGC types project to distinct SC regions and provide inputs to multiple types of SC neurons.[15–17]

Single-cell RNA sequencing (scRNA-seq) and single-nucleus RNA sequencing (snRNA-seq) have been widely used in the central nervous system (CNS) to characterize cellular heterogeneity and the dynamic changes of specific cell populations over time. Here we performed snRNA-seq analysis of the mouse SC isolated at various ages during the first month of postnatal life to characterize SC cell subtypes across development. Our results revealed molecularly distinct excitatory and inhibitory neuronal subtypes, many of which reside exclusively in specific SC laminae or project to specific brain regions. Moreover, we find neurons and glial cells express genes associated with axon guidance, targeting, and synapse formation in a temporally defined manner. For convenient access to these data, we have created a user-friendly web portal that allows for comparative gene expression analyses in these data across development: https://parklabmiami.shinyapps.io/superior-colliculus-snRNAseq/.

RESULTS

Single-nucleus profiling of developing and mature mouse SC

Some cell types, such as neurons, are more susceptible to tissue dissociation processes and are underrepresented in scRNA-seq data. In contrast to whole cells, nuclei are more resistant to mechanical insult and can be isolated from frozen tissue.[18] Indeed, studies have revealed that snRNA-seq profiling can provide an unbiased survey of neural cell types, and, as a result, snRNA-seq has become a popular choice for profiling susceptible cells such as neurons.[19]

To profile gene expression of SC during development and maturation, we analyzed the transcriptomes of single nuclei across four time points: embryonic day 19 (E19), postnatal day (P) 4, P8, and P21. We selected these time points because, together, they encompass discrete yet overlapping developmental events, including axonal outgrowth, axonal targeting, topographic mapping, synaptogenesis, oligodendrocyte differentiation, myelination, and

synaptic refinement and maturation. For each age, we micro-dissected the SC territory from several animals, which were pooled. After detergent-based digestion and mechanical dissociation followed by nuclei isolation using sucrose density gradient centrifugation, the single-nucleus suspension was sequenced using the 10X Genomics droplet-based snRNA-seq platform (Figure 1A). Downstream clustering and analyses were done using Seurat and the Bioconductor suite of bioinformatics tools. After stringent quality control (Figure S1), a total of 9,728 high-quality nuclei (2,585 from E19, 2,386 from P4, 2,508 from P8, and 2,249 from P21) were retained for downstream analysis. An average of 10,451 unique molecule identifiers (UMIs) were captured per nucleus (7,457 for E19, 9,882 for P4, 10,961 for P8, and 13,928 for P21) and an average of 3,535 genes were detected per nucleus (3,030 for E19, 3,574 for P4, 3,644 for P8, and 3,953 for P21) (Figure S1B).

Identification of cell types in the developing mouse SC

To identify shared and unique cell types across SC development, we used the Seurat integration pipeline to jointly analyze cells from all four time points and perform unsupervised clustering (see STAR Methods). Projection of cells onto Uniform Manifold Approximation Projection (UMAP) plots[20] revealed structures suggestive of cell lineage and differentiation (Figures 1B and 1C). Using the top differentially expressed genes (DEGs) per cluster and a panel of previously described cell type marker genes (e.g., *Slc17a6, GAD1, Aqp4, Gfap, Cspg4, Bmp4, Mbp, Mki67, P2ry12, Cldn5, Col1a1*, and *Cdh1*; Figures 1D and 1E), we identified 21 neuronal and 10 non-neuronal cell clusters. These clusters represented most major cell types known to comprise the SC, including neurons, astrocytes, microglial cells, and oligodendrocyte-lineage cells, as well as endothelial and vascular leptomeningeal cells (Figures 1B and 1D).

Consistent with the notion that neuronal nuclei are expected to survive the dissociation protocol, neurons constituted about 77% of all cells identified. Among all neuronal cells, 54% were excitatory neurons and 46% were inhibitory neurons, but this ratio varied by time point. While neurons at E19 and P4 were approximately 60% excitatory and 40% inhibitory, neurons at P8 and P21 were approximately 46% excitatory and 54% inhibitory (Figure 1F). These observations are in line with previous studies showing the changes in the ratio of excitatory to inhibitory neurons during development.[21] In addition, consistent with the timing of oligodendrocyte differentiation and myelination, the proportion of mature *Mbp*$^{+}$ oligodendrocyte-lineage cells was higher in P8 and P21 than E19 and P4. We also observed that the proportion of non-neuronal cells, such as microglia and astrocytes, gradually increased over time. Altogether, these results corroborate prior studies investigating the cell type composition of the brain throughout early postnatal development and further support the use of snRNA-seq to study SC cellular heterogeneity.[19,22,23]

Heterogeneity of SC neurons across development

Several studies have described molecularly distinct types of adult SC neurons, but a genome-wide characterization throughout development remains lacking. Because neurons made up a sizable percentage of our dataset, we were well positioned to provide a reference map of the transcriptional heterogeneity among SC neuronal subtypes. To this end, we performed a nested cluster analysis using only neurons so that only genes variably expressed among

neurons were considered. This resulted in 25 neuronal clusters (Figures 2A and S2A), which, when projected onto a UMAP (Figure 2A), were principally segregated by excitatory or inhibitory subtype as confirmed by expression of the gene *Slc17a6*, which encodes the vesicular-glutamate transporter VGlut2, or by expression of glutamate decarboxylase genes, *GAD1* and *GAD2*, respectively (Figures 2C and 2D). These neuron clusters were therefore annotated as EN1-13 or IN1-12 subtypes. We then pivoted the data to measure neuronal subtype quantities across developmental ages and found that most subtypes were detected at most time points (Figures 2B, S2B, and S2C). However, subtypes EN1 and IN1 were preferentially enriched at earlier time points E19 and P4, and many subtypes increased in proportion at later time points P8 and P21. At the extreme, some subtypes were temporally restricted, such as subtype EN7, which was found only at E19 and P4 stages (Figure S2C).

Subsequent differential expression (DE) analysis revealed both distinct and overlapping marker genes across subtypes (Figure 2D). While some neuron subtypes could be uniquely identified by the expression of a single gene, such as *Etv1* expression by EN13 and *Maf* by IN12, other subtypes were better described using combinations of multiple genes, similar to the approach taken in a previous study that classified SC neurons using multiple molecular markers.[24] For example, subtype EN7 can be specified by joint expression of *Kitl* and *Slc18a6*, and subtype IN10 can be specified by joint expression of *Ebf3* and *Gata3*. Given the varying degree of marker specificity, we next quantified subtype expression profile similarities through a dendrogram analysis (Figure S2D). While our results re-emphasized principal neuronal class (excitatory vs. inhibitory) as the greatest source of variation, we also observed that some neuron subtypes, such as EN1 and IN1, were less distinct than others. We confirmed this observation by counting the number of DEGs per neuronal subtype grouped by neuronal class and found that, indeed, subtypes EN1 and IN1 had the fewest numbers of DEGs, while other, more distinct subtypes had upwards of 100 DEGs (Figures S2E and S2F).

Correlates between excitatory subtype markers and SC laminae

Previous studies have demonstrated that morphologically and physiologically distinct types of excitatory SC neurons are localized in distinct laminae and contribute to various behavioral responses in mice.[9,25] From our initial DE analysis, we next performed a more detailed inspection of the marker genes that distinguish the excitatory subtypes. Among the 13 excitatory neuronal subtypes, we found subtypes that exhibit enriched expression of genes that are already known to label subpopulations of SC neurons (Figure 2D). Subtype EN13 expressed *Etv1* exclusively, a gene known to be expressed in a subpopulation of neurons in the SO layer.[24] *Gfra1* was also highly expressed in this subtype. A previous study has shown that *Pitx2* defines a subpopulation of excitatory neurons in the stratum griseum intermediate (SGI).[26] We found that subtype EN8 expressed elevated levels of *Pitx2* and *Gli3* compared to other excitatory subtypes (Figures 2D and S8E). Thus, EN8 likely represents this previously characterized SGI cell type. Other subtypes with notable gene enrichment were EN12, which was enriched for *Egflam* and *Tmem132c* expression, and EN11, which was enriched for *Nfib* and *Nfix*.

Given the topographic arrangement of SC neurons, we next examined whether these neuronal subtypes were localized in discrete laminae in adult SC. In the Allen Brain *in situ* hybridization database, *Gfra1*, which we found to be expressed in excitatory neurons and particularly highly in EN6, was detected highly in the SGS and less densely in the deeper layer (Figures 2E and 2F). *Egflam*, a marker for EN12, was detected predominantly in the SO (Figure 2E). *Kitl*, a gene expressed highly in EN5, EN6, and EN7, is found mostly in the SGS. Similarly, *Tcf7l2*, which was highly expressed by EN2 and EN7, was enriched in the SGS and SO. To validate the layer-specific expression of these marker genes in the mouse SC, we performed fluorescent *in situ* hybridization (FISH) against *Gfra1* and *Slc17a6*, the gene encoding VGlut2 (Figure 2F). In the SGS layer, where *Gfra1* expression is predominant within the SC, we found that approximately 90% of *VGlut2*+ cells co-labeled with *Gfra1* and nearly all *Gfra1*$^+$ cells co-labeled with *VGlut2*. Conversely, in the deeper layers of the SC (i.e., SGI), where *Gfra1*$^+$ cells are less abundant, less than 10% of *VGlut2*+ cells co-label with *Gfra1*. These results are consistent with our snRNA-seq data and suggest that certain neuron subtypes identified in our analyses are enriched in specific layers.

Correlates between inhibitory neuron subtype markers and SC laminae

As with the excitatory neuron subtypes, our cluster analysis identified 12 distinct inhibitory neuronal subtypes with distinct transcriptional signatures (Figure 2A) whereby most subtypes could be identified by a single or a combination of genes. For example, *Spon1* was specific to IN6, *Meis1* and *Gulp1* co-expression was specific to IN7, and subtype IN11 could be defined by high expression of *Fibcd1* and *Pax7* (Figure 2D). We examined whether inhibitory neuron subtype marker genes displayed SC layer specificity, again referring to *in situ* hybridization (ISH) data from the Allen Brain Atlas. We found that *Nos1ap*, a marker for IN3, was detected primarily in the SGS (Figure 2E) and that *Spon1*, a marker for IN6, was enriched in the SGS and SO (Figure 7K). Other marker genes, such as *Meis1*, which was highly expressed by IN7 and detected in the SGS and SO, were found in multiple SC layers. Altogether, these data demonstrate that cluster analyses can identify transcriptionally distinct neuron subtypes with specific anatomical localizations within the layers of the SC.

Changes in neuronal gene expression across development

Critical neurodevelopmental processes, such as axon growth, axon targeting, retinotopic mapping, and synapse formation and maturation, require temporally regulated expression of gene products such as transcription factors and cell adhesion molecules. To better understand these dynamics, we analyzed DEGs across time. For both excitatory and inhibitory neuron classes, genes such as *Nnat, Nsg1, Nsg2, Fam171a2, Basp1, Pcsk1n*, and *Rtn1* were enriched at E19 (Figures 3A and 3B). Likewise, the transcription factor *Tcf7l2*, whose gene product plays a key role in Wnt signaling, was highly upregulated at P4 for both classes. Further characterization of the combined neuronal gene expression changes with Gene Ontology (GO) analysis demonstrated the downregulation of genes associated with Wnt signaling from P4 to P8, supporting the importance of temporally controlled Wnt during this period (Figures S3A and S3B). Interestingly, we observed that the greatest number of neuronal gene expression changes occurred between P8 and P21 (Figure 3C), where P21 was enriched for genes such as *Lncpint, Specc1, Rasgrf1, Naaladl2, Aifm3*, and *Pcgf5*. The overt changes during this period may reflect neuronal developmental

processes associated with synaptic maturation and the appearance of oligodendrocytes and myelination (Figure 1F). Indeed, our GO analysis of genes upregulated from P8 to P21 revealed terms such as “regulation of synaptic plasticity” and “synaptic vesicle exocytosis” (Figure S3B). Overall, both excitatory and inhibitory neurons showed similar temporal patterns of transcriptional activity whose inferred biological functions through GO analysis recapitulate known developmental milestones.

Examination of Allen Brain *in situ* data revealed that some genes are regulated in both spatial and temporal fashion. For example, excitatory neurons showed high expression of transcription *Zic1* at P4. *In situ* data showed that, at E18.5 and P4, *Zic1* expression was high only within the medial side of the SC in the SGI layer and not present in the lateral side (Figure 3D, top three panels). By adulthood (i.e., P56), medial specific *Zic1* expression in the SC was no longer detected (Figure 3D, bottom panel). This expression pattern suggests that *Zic1* may determine axon directionality along the lateral-medial axis in this region (see discussion). Similarly, the transcription factor *Lef1* was highly expressed at P8 and, in addition to areas of the thalamus, was almost exclusively detected in SC (Figure 3E). These data support the notion that neuronal gene expression changes are spatiotemporally regulated.

With these findings, we next asked whether developmentally regulated gene expression programs could be identified at the subtype level as opposed to at the level of principal neuronal class. To address this, we used Monocle3 to perform trajectory analysis (see STAR Methods). Our results revealed several trajectories branching from a central “node” where cells with the earliest projected pseudotimes were enriched for neuron subtypes EN1 and IN1, which were most prevalent at E19 and P4 (Figures S4A and S4C). Furthermore, we observed that cells further along the pseudotemporal progression were also enriched for cells collected at later time points P8 and P21 (Figure S4B).

With these trajectories, we identified 9,725 genes that differed as a function of pseudotime. We then clustered these genes into modules and subsequently found one gene module to be specific to a trajectory traveling from IN1 to IN8, and from IN8 to IN4 (Figure S4D). Among the top statistically significant genes in this module were *Epyc, Il1rapl2, Kcnip1*, *Pax7, Pax3*, and *Ptprt* (Figure S4E). Interestingly, although *Pax7* increased in expression further along the trajectory, *Pax3* was detected transiently early in the trajectory and in opposition to *Pax7*, agreeing with a previous study demonstrating divergent expression patterns between these two transcription factors during development.[27] These results present a potential IN1-IN8-IN4 developmental trajectory that possibly could be mediated by transcription factors such as *Pax7* and *Pax3*.

Changes in glial gene expression across development

In addition to neurons, we successfully captured virtually all glial cells, of which astrocytes were the most abundant. Comparisons of astrocyte gene expression across the developmental time points (Figure S5A) revealed an enrichment of axon guidance molecule genes, such as *Ephb1, Robo1*, and *Ephb2*, at E19 and their decreased expression overtime. Additionally, P4 astrocytes highly expressed *Hs6st3*, a heparan sulfate (HS) sulfo-transferase known to modify HS and regulate adhesion. P8 astrocytes were enriched for *Ptchd4*, a repressor of

canonical hedgehog signaling, and glutamate metabotropic receptor *Grm7*. Like neurons, astrocytes also demonstrated a large increase in the number of DEGs between P8 and P21 (Figure S5B). Among them were genes such as *Gja1* and *Gjb6*, encoding the gap-junction proteins also known as Connexin-30 and Connexin-43, respectively, which map to the GO term "cell junction assembly" (GO: 0034329). These genes have been implicated in astroglial synapse coverage.[28] Other genes important for astrocytic function, such as those that encode ion channels and ion channel regulators (e.g., *Trpm3* and *Lgi1*) and phospholipases (e.g., *Plcb1* and *Gpld1*), were also upregulated at P21. These results collectively suggest that astrocytes may play a role in axon guidance early in postnatal development and reaffirm their roles in synaptic refinement in young adulthood concurrent with the appearance of mature *Mbp*$^{+}$ oligodendrocyte-lineage cells by P21.[29]

Oligodendrocyte-lineage cells showed UMAP coordinates that were suggestive of differentiation across development (Figure 1B). In agreement with this observation, our DE analysis showed an enrichment of oligodendrocyte progenitor cell (OPC) marker genes such as *Olig1* and *Pdgfra* at E19 and a strong upregulation of genes whose products encode for components of the myelin sheath, such as *Mag, Plp1, Mbp*, and *Mog*, at P21 (Figure S5C). Moreover, we observed that *Sox6* expression remains high from E19 to P8 but is downregulated at P21. This is consistent with the notion that Sox6 maintains the precursor state of oligodendroglial cells, thereby ensuring the proper timing of myelination in the CNS.[30] Other genes showed a similar expression pattern, such as *Lrrtm4* and phosphodiesterase *Pde4d*. Overall, as for other cell types, we observed substantially more genes differentially expressed between P8 and P21 than compared to other time points, again suggesting that this critical period is highly transcriptionally dynamic (Figure S5D).

Although we successfully identified a microglia cluster, they totaled 90 nuclei, reducing our power to identify DEGs. Thus, their analysis was not included in this report.

Comprehensive assessment of major axon guidance molecules

Cadherins and protocadherins—Cadherins and protocadherins play important roles in axon guidance and target selection. Among the cadherin family members, we found that the expression of *Cdh8, Cdh12, Cdh13*, and *Cdh18* was particularly high in neurons and low in non-neuronal cells (Figure 4A). In contrast, we observed significant expression of specific cadherin genes in non-neuronal cells; *Cdh20* expression was exceptionally high in astrocytes, whereas *Cdh1* expression was specific to epithelial cells. We found that *Pcdh9* and *Pcdh15* were highly expressed in the oligodendrocyte-lineage cells. Notably, *Pcdh10* and *Pcdh15* were expressed at higher levels in the excitatory than inhibitory neurons. On the other hand, *Pcdh7* expression was higher in the inhibitory neurons (Figure 4A). During our analysis, we noticed that, while most cadherins and protocadherins were expressed at similar levels in excitatory and inhibitory neurons as a class, their expression varied highly at the subtype level. Since selective cadherin expression has been shown to promote neuron class-specific cell adhesion and synaptic connection,[31,32] we generated a comprehensive panel of cadherin and protocadherin family gene expression across neuronal subtypes (Figure 4B and S6). From this panel, we found that *Cdh7* was expressed at higher levels in subsets of excitatory neurons (EN5 and EN6). Previously, Byun et al. described *Cdh7* as a marker for

a subpopulation of neurons in the upper SGS (uSGS).[24] We extend this finding to show that *Cdh7* is a marker for excitatory neurons in the SGS. We further validated this result with two-color FISH (Figure 4C), which shows *Cdh7* expression predominantly in the *VGlut2*+ cells. Conversely, we found that *Cdh12* and *Cdh22* (Figures 4A and 4D) were preferentially enriched in inhibitory subtypes compared to excitatory populations.

Eph receptors and ephrins—This family of receptors and ligands are key signaling molecules involved in retinocollicular topographic mapping. Accordingly, many Eph receptors were highly detected in the SC neurons across multiple time points with the exception of *Epha1, Epha2, Ephb3*, and *Ephb4* (Figure S7A). Multiple ephrin ligands were also detected, and some, such as *Efna2*, and *Efnb3*, showed downregulation in neurons over time. Overall, we observed that genes from the Eph receptor and ephrin family were primarily expressed in neurons compared to non-neuronal cells. Some exceptions to this included astrocytic expression of *Epha5, Ephb1*, and *Ephb2*, which decreased significantly over time, and *Efnb3* expression by oligodendrocyte-lineage cells.

Semaphorins and plexins—These molecules regulate functions related to cell morphology and communication that contribute to axon guidance. In our data, most semaphorin-plexin family genes were detected in SC neurons across all time points, such as *Plxna4, Sema4f*, and *Sema4g* (Figure S7A). Although neurons maintained constant expression levels of most of these genes, *Sema3f* and *Plxna1* showed a significant decrease across developmental time points. However, non-neuronal cells also expressed members of the semaphorin-plexin family. For example, astrocytes demonstrated enriched expression of *Plxnb1* and a strong upregulation of *Sema4b* overtime, and oligodendrocyte-lineage cells showed similarly strong temporal changes in *Plxnb3, Sema4d*, and *Sema6d*.

Robo receptors and Slit—While transcripts for *Robo1* and *Robo2* were detected in nearly all cell populations, these genes were most highly expressed in SC neurons (Figure S7A). In contrast, *Robo3* was detected at low levels in all cell types at all time points except for in excitatory neurons, whose expression significantly increased across the time points. Further inspection of *Robo3* showed that its expression was limited to neuron subtypes EN5 and EN6, subtypes whose proportions correspondingly increased over time. Interestingly, these same *Robo3*$^+$ subtypes comprised a subset of *Gfra1*$^+$ neurons. Two-color FISH showed *Robo3* expression in *Gfra1*$^+$ cells, further corroborating our sequencing results (Figure S7B). Conversely, while the Robo ligands *Slit2* and *Slit3* were most highly detected in epithelial cells and only moderately expressed by SC neurons, *Slit1* was almost exclusively expressed by neurons (Figure S7A). Given the role of the SLIT-ROBO pathway in the guidance of RGC axons through the optic chiasm and to the brain, we also queried mouse RGC scRNA-seq data from the Broad Institute's Single-Cell Portal. We found that *Robo1* expression was particularly high in a few RGC clusters, while *Robo2* expression was high and uniform across all RGC subtypes. On the other hand, *Robo3* was detected at low levels. In summary, these data suggest that multiple cell types, including specific neuron subtypes of the SC, could affect the targeting and innervation of axons to the SC.

Correspondence between neuronal subtypes and published SC scRNA-seq data

Several recent studies have profiled murine SC neurons using scRNA-seq or snRNA-seq. Two of these studies elegantly utilized transsynaptic and retrograde adeno-associated virus (AAVs) to specifically profile retinorecipient neurons and SC projection neurons, respectively. Tsai et al. developed the Trans-seq method, which used modified AAV-wheat germ agglutinin (WGA) to identify and profile SC neurons that are post-synaptic to RGCs.[33] Cheung et al. developed virally encoded connectivity transgenic overlay RNA sequencing (Vector-seq) using retrograde viruses to profile SC projection neurons that send axons to different brain regions.[34] In 2021, Xie et al. performed snRNA-seq of the adult mouse SC and developed an informatics tool called spatial classification of mRNA expression data (SPACED) to compute layer-specific probabilities for neuron subtypes identified in their study.[22] Across all studies, the authors provided novel user-defined subtypes of SC neurons. How these subtypes compare across studies is not known, and whether these populations are detected in our development time-course dataset is unclear.

To elucidate unified molecular definitions of SC neuron subtypes, we pulled data from each study and first asked whether neuronal subtypes as defined in our study were detected in these published data. To this end, we applied the SingleR classification algorithm[35] (Figure 5A) using the snRNA-seq data in our study as a reference and data from these previous datasets as query sets. Briefly, the SingleR algorithm computes Spearman correlations between cells of the query data and cells of the reference data on the subset of marker genes for subtypes of the reference data (i.e., EN1-13 and IN1-12 subtype marker genes). Per-subtype scores are determined from these correlations, and the subtype with the highest score becomes the predicted subtype (see STAR Methods for further details). This approach is especially suitable for this analysis given the differences in sequencing depth and dissociation method, study-associated batch effects, and technical noise driven by ambient RNA contamination.

The original Trans-seq study categorized retinorecipient SC neurons into three excitatory subtypes (ESC1–3), and five inhibitory subtypes (ISC1–5).[33] To compare these subtypes against subtypes from our study, we applied SingleR and computed the proportions of predicted labels that comprised each of the Trans-seq subtypes (Figures 5B and 5C). Our analysis showed that more than 93% and 97% of cells in Trans-seq ISC1 and ISC2 subtypes, respectively, were predicted to be our inhibitory subtype IN3. This suggests a high degree of similarity between these three populations and perhaps that IN3 may be a retinorecipient population. Conversely, only excitatory neuron subtypes EN5, EN6, EN9, and EN12 had predictions that comprised more than 10% of any Trans-seq subtype. This is in line with the expectation that retinorecipient neurons comprise only a subset of all SC neurons and further suggests that RGCs only project onto SC neurons in a subtype-specific manner. Overall, five neuronal subtypes (IN3, IN9, EN12, IN4, and EN5) comprised approximately 75% of predicted subtypes in the Trans-seq dataset (Figure 6A), indicating that these subtypes may represent most likely candidates of RGC post-synaptic input.

The Vector-seq study by Cheung et al. used snRNA-seq to profile about 55,000 nuclei of the SC. When we applied the same SingleR approach to these data, we found strong concordance between our neuron subtypes and Vector-seq clusters. Of 35 Vector-seq

clusters, 13 had greater than 90% of its cells predicted to be of a single neuron subtype as defined in our study and 20 were composed of more than 70% of a single subtype (Figures 5D and 5E). Notably, using their retrograde labeling strategy, Cheung et al. reported that approximately 1,500 Vector-seq excitatory neurons (clusters 2 and 7, Figure 3C from Cheung et al.) were SC neurons that project to contralateral paramedian pontine reticular formation (PPRF) (i.e., SC neurons that are known to control orientating movements), and about 3,100 cells were SC neurons (clusters 10 and 11, Figure 3C from Cheung et al.) that project to the thalamic lateral posterior nucleus (LP). We repeated SingleR analysis on only excitatory neurons and found that Vector-seq excitatory neuron cluster 7 had high concordance with our excitatory subtype *Pitx2*$^{+}$ EN8, suggesting that EN8 likely represents SC neurons projecting to the PPRF (Figures S8A, S8B, and S8E). Moreover, Vector-seq excitatory neuron cluster 10, which is *Ntng2*$^{+}$, was comprised mostly of *Ntng2*$^{+}$ excitatory subtype EN3, while Vector-seq excitatory neuron cluster 11 was made up of a combination of EN2 and EN12, which could be distinguished by *Cbln2* (Figures S8C and S8D). From this, we speculate that subtypes EN3, EN2, and EN12 are SC neurons that project to the thalamic LP.

Finally, we applied SingleR to scRNA-seq data of the adult SC by Xie et al.[22] Using these data, we clustered neuronal cells and computed their concordance to neuron subtypes identified in our study. We found that 14 of the 22 clusters had over 75% of their predicted subtype compositions to be of a single neuron subtype (Figures S8F and S8G), suggesting high concordance between the subtype heterogeneity evaluated in both studies. When comparing marker genes against the mouse SC snRNA-seq clusters identified by Xie et al. (different from clusters compared in SingleR analysis; see STAR Methods for details), we again found good correspondence between the two studies. For example, clusters Ex-6 (i.e., *Gpc3*$^{+}$ neurons) and Ex-8 (i.e., *Sntb*$^{+}$ neurons) from Xie et al. corresponded to our EN12 and EN6, respectively (Figures 5F and 5G).

While the SingleR approach allows for mapping cell identities from a reference dataset to an unlabeled query dataset, direct integration analysis of cells across all studies would allow for a more comprehensive view of SC neuronal heterogeneity. Thus, we integrated neurons from Cheung et al., Tsai et al., and the current study using Seurat and examined subtype distribution and overlap. Our results demonstrate that most neuronal subtypes identified in our analysis cluster together with the neuronal clusters identified by Cheung et al. using Vector-seq (Figures 6B, 6C, and 6D). Of note, Tsai et al. used Trans-seq to isolate retinorecipientSC neurons. Interestingly, subtypes ISC1 and ISC2 by Tsai et al. clustered with IN3 from our analysis and cluster 4 from Cheung et al., suggesting that these inhibitory neurons may be recipients of retinal projections.

Using *in situ* hybridization and immunostaining, Byun et al., demonstrated that several molecular markers collectively categorize 10 superficial SC (sSC) neuronal types, including the genes *Rorβ* and *Etv1*. As mentioned previously, we found that *Etv1* expression was unique to EN13. Several subtypes from both excitatory and inhibitory populations in our study expressed *Rorβ*, albeit the expression was more widespread in the excitatory neuron clusters (Figure 6E). On the other hand, we found that *Etv1* expression was unique to EN13.

Previous studies have also classified inhibitory SC cells into three non-overlapping categories in mice; those that express *Sst, Vip*, or *Pvalb*. *Pvalb*$^+$ neurons, which are found in the lower SGS and SO,[36] innervate the LP of the thalamus. Thus, some *Pvalb*$^+$ neurons are projection neurons, as opposed to interneurons.[37,38] While *Pvalb* marks a specific subclass of GABAergic fast-spiking inhibitory interneurons in the cerebral cortex, striatum, and hippocampus,[39] it was shown that *Pvalb*$^+$ neurons in the sSC present heterogeneous spiking profiles and morphologies, and only a fraction contained GABA. On the other hand, a higher proportion of the *Pvalb*$^+$ population in the intermediate layers of the SC showed the presence of GABA. Consistent with the notion that *Pvalb*$^+$ neurons in the SC are likely heterogeneous populations of both glutamatergic and GABAergic neurons,[40] we observed low but detectable levels of *Pvalb* across multiple neuronal subtypes (Figure 6E). Conversely, we found that *Sst* and *Vip* labeled specific subtypes; *Sst*$^+$ neurons corresponded to subtypes IN4, IN8, and IN12, while *Vip*$^+$ neurons corresponded to subtype IN9.

Characterization of a subpopulation of GABAergic neurons: Pax7-expressing neurons

The SGS contains a high density of GABAergic neurons; 30% of all neurons in this region are GABAergic,[41] and approximately one-third of the post-synaptic targets of retinotectal terminals are GABAergic.[42] GABAergic SC neurons and their connections with other brain regions have been shown to play a critical role in wakefulness and eye movements.[43,44] However, the development and functional organization of GABAergic SC circuits is still under investigation. Several GABAergic SC cell types have been described based on axon projections, orientation of dendritic arbors, and/or the colocalization of a variety of immunocytochemical markers.[42,45–47] In our analysis, we identified *Pax7* as a GABAergic neuron-selective marker, which was detected in subtypes IN2, IN4 IN6, IN9, IN11, and IN12 (Figures 7A and 7B). Pax7 is a transcription factor known to direct embryonic cells along a neurogenic lineage and form the SC boundary. Based on the Allen Brain ISH database, in the adult mouse brain, Pax7 expression is highest in the sSC (Figures 7C and 7D). To investigate the organization of *Pax7*$^+$ GABAergic neurons in the SC, we injected AAV-FLEX-GFP into the sSC of adult Pax7-Cre mice in which GFP expression is limited to the Pax7-expressing cells. Of note, Pax7-Cre mice crossed to Rosa26-Tomato reporter mice showed tdTomato expression predominantly in the midbrain, and not in the cortex (Figure 7E), consistent with the Pax7 expression pattern shown in the Allen Brain Atlas (Figure 7C). Interestingly, we found GFP$^+$ axon terminals in the ventral LGN (vLGN) but not in the LP, parabigeminal nucleus (PBg), or dorsal LGN (dLGN) (Figures 7F–7H). On the other hand, Gale et al. selectively labeled inhibitory neurons in the sSC using GAD2-Cre mice and demonstrated axon terminals in several nuclei, including the PBg, the dorsolateral portion of dLGN, and the vLGN.[45] This suggests that only certain inhibitory neurons are *Pax7*$^+$ as in our cluster analysis. Next, we performed two-color FISH to determine whether *Pax7* could be colocalized with a second inhibitory neuron subtype marker and investigate whether *Pax7*$^+$ neurons were composed of multiple inhibitory subtypes. For this experiment, we selected *Spon1* (for IN6) and *Fibcd1* (for IN11) due to their enrichment in the SGS according to the Allen Brain Atlas. Our findings confirmed that *Spon1* and *Fibcd1* are expressed in *Pax7*$^+$ cells and indeed localized to the SGS layer (Figures 7I and 7J). We further confirmed these results against ISH data from the Allen Brain Atlas (Figures 7K and 7L). Together, these results indicate that *Pax7* labels a heterogeneous population of

GABAergic SC neurons, composed of at least two transcriptionally distinct subtypes with long-range projection to the vLGN.

DISCUSSION

The SC is a region of multisensory integration and a rising model for studying circuit formation. During SC development, distinct transcription factors, cell adhesion molecules, and extracellular matrix proteins contribute to axon guidance and formation of proper neural circuits. In our analysis, we identified *Zic1* as one such transcription factor with strict spatial and temporal developmental regulation (Figure 3D). It has long been known that members of the Zic family of zinc-finger transcription factors regulate the expression of axon guidance molecules and play critical roles in axon targeting in the CNS. For example, Zic2 controls the expression of EphB1 receptors in select populations of RGCs in the retina, which in turn promotes projection of these neurons to the ipsilateral brain side.[48] Given our findings, one might hypothesize that Zic1 plays a role in guiding incoming axons to proper regions in the SC. Our analysis also identified the adhesion molecule gene *Cdh22*, which we found to be specific to inhibitory neurons. Previous studies have shown that certain cadherin members have a function specifically in interneurons, particularly at the inhibitory synapses; Cdh13 deficiency was shown to reduce synapse turnover, producing an increase in inhibitory synapse density.[49] It is plausible that Cdh22 plays a similar role and regulates interneuron development and synaptic function in the SC.

Recent studies have demonstrated that glial cell expression of axon guidance molecules also plays a critical role in the formation and maturation of CNS circuits. For example, astrocytes have been shown to secrete a variety of growth factors and extracellular matrix proteins that modulate the direction of axon growth and extent of synapse formation.[50] Supporting this notion, our data showed dynamic changes in astrocytic expression of various guidance molecules across time points; while genes encoding Eph receptor and ephrin molecules showed decreased expression over time, subsets of genes from the semaphorin-plexin signaling pathway, such as *Sema4a* and *Sema4b*, increased in expression. Further functional studies will be needed to dissect the precise role of astrocytes in SC circuit maturation.

The SC contains a heterogeneous population of GABAergic neurons whose properties and innervation play a key role in the regulation of collicular functions. We showed that *Pax7* transcripts are enriched in subpopulations of inhibitory neuronal sub-types (i.e., approximately half of all inhibitory neurons in the SC). By labeling axons from $Pax7^+$ neurons in the sSC, we found that these neurons send long projections exclusively to vLGN and not to other known distal targets (e.g., LP, dLGN, and PBg).[8,45] The vLGN is thought to be a part of a multimodal system, receiving retinal afferents but establishing subcortical interconnections with non-imaging forming areas (e.g., olivary pretectal nuclei, accessory optic system, and suprachiasmatic nuclei).[51] The vLGN also projects to the SC, the periaqueductal gray area (PAG), and the nucleus reuniens of the ventral midline thalamus. These regions all contribute to behavioral responses to visual threats.[52,53] Whether $Pax7^+$ sSC neurons are a functionally distinctive population of cells that subserve visually guided behavior or non-image-forming visual functions remains unknown.

In summary, this report provides a comprehensive molecular characterization of the cell types that comprise the SC across murine development, with particular emphasis on neuronal heterogeneity and molecules involved in circuit assembly. By comparing *in situ* hybridization data from the Allen Brain Atlas, we demonstrate that certain transcriptionally defined neuronal subtypes also display anatomic specificity. We also attempt to provide a unified definition of neuronal subtypes of the SC across multiple studies and to infer subtype-specific projections to various brain regions. Finally, by leveraging our snRNA-seq data, we confirm and characterize projections from the $Pax7^{+}$ subset of SC neurons to demonstrate the utility of these data as a starting point for manipulations in specific neuronal populations and circuits. To this end, we have provided a web portal for exploration of these data: https://parklabmiami.shinyapps.io/superior-colliculus-snRNAseq/.

Limitations of the study

While the SC of mice is relatively large, we cannot rule out that, through manual dissection, we also retained contamination from deeper brain regions, particularly for E19 brain samples, in which the SC is structurally less defined. As this may lead to sampling variability, a more precise approach may include the use of tracers. Furthermore, the number of cells sequenced in our study is relatively low (approximately 9,700); the study by Cheung et al. sequenced around 55,000 neurons. While our analyses demonstrated substantial similarities in neuronal heterogeneity between studies, having fewer cells can limit detailed examination of DE across conditions. These two sources of sampling variability may be abrogated by including additional biological replicates (i.e., more sequenced samples per time point). An alternative approach may be to sample SC cells at shorter increments in time, which would also have the added benefit of capturing intermediate cell states across developmental processes and allow improved bioinformatic modeling through trajectory analyses. Finally, as with many scRNA-seq studies, further experimental validation is needed. While we have validated some neuron subtype markers to specific brain regions such as with Pax7, the identity, distribution, and function of neuron subtypes with less distinct molecular profiles remain unclear. Likewise, how the expression of specific axon guidance molecules affects neuron subtype circuitry requires functional studies. Nevertheless, descriptive studies on cellular transcriptional heterogeneity provide a roadmap for investigating the molecular determinants of brain circuitry.

STAR★METHODS

RESOURCE AVAILABILITY

Lead contact—Further information and requests for resources and reagents should be directed to and will be fulfilled by the Lead Contact, Kevin K. Park at kpark@miami.edu.

Materials availability—This study did not generate new unique reagents.

Data and code availability

- Original single-nucleus RNAseq data have been deposited at Gene Expression Omnibus (GEO) with the Accession number: GSE224407 and are publicly **available** as of the date of publication. This paper also analyzes existing,

publicly available data. These accession numbers and datasets are listed in the key resources table.

- All original code has been deposited at Zenodo (10.5281/zenodo.8061024) and is publicly available as of the date of publication. DOIs are also listed in the key resources table. Original code has also been deposited at https://github.com/ParkLabMiami/snRNAseq-developing-superior-colliculus.
- Any additional information required to reanalyze the data reported in this paper is available from the lead contact upon request.

EXPERIMENTAL MODEL AND STUDY PARTICIPANT DETAILS

Animals—All animal experimental procedures were performed in compliance with protocols approved by the Institutional Animal Care and Use Committee (IACUC) at the University of Miami Miller School of Medicine. Animals used were C57BL/6J (The Jackson Laboratory, stock# 000664), Pax7-Cre (The Jackson Laboratory, stock# 010530), and R26 loxP-STOP-loxP-tdTomato (a gift from Dr. Fan Wang, Massachusetts Institute of Technology). All animals were housed in a viral antigen-free facility and kept under standard 12-h light-dark conditions. For all surgical procedures, mice were anesthetized with ketamine and xylazine. For analgesia, buprenorphine (0.05 mg/kg) was administered post-operatively. Animals of both sexes were used unless specified.

METHOD DETAILS

Nuclei isolation and analysis of single-nucleus RNAseq—Nuclei were isolated from SC using detergent-based digestion and mechanical dissociation followed by a sucrose density gradient.[19] Briefly, SC from E19, P4, P8, and P21 mice were manually isolated and homogenized in RNAase-free lysis buffer (0.32 M sucrose, 3 mM $CaCl_2$, 3 mM $MgAc_2$, 0.1 mM EDTA, 10 mM Tris-HCl,1 mM DTT, 0.1% Triton X-100 in DEPC-treated water) using a glass Dounce homogenizer on ice. For each sample, SC were collected from multiple mouse donors and pooled (i.e., two mice for E19 and five mice for all other time points). Care was taken to micro-dissect SC regions specifically without substantial contamination from deeper brain regions, particularly for the E19 brain in which the SC is less defined structurally. Animals of both sexes were used for all ages except for E19 which were all males. The homogenate was loaded into a polycarbonate ultracentrifuge tube containing sucrose solution (1.8 M sucrose, 3 mM $MgAc_2$, 1 mM DTT, 10 mM Tris-HCl in DEPC-treated water) in the bottom and centrifuged at 107,000 g for 2.5 h at 4°C. Supernatant was aspirated, and the nuclei containing pellet was incubated in RNAse-free 1x PBS, 0.04% BSA, 0.2 U/μL RNAse inhibitor on ice before resuspending the pellet. The nuclear suspension was filtered twice through a 30 μm cell strainer and counted using a Nexcelom Cellometer K2 before performing single-nucleus capture on the 10X Genomics 3′ v3 single cell RNA-Seq. Target capture of 2,000 nuclei per sample was used and the 10 × 3′ v3 scRNA-Seq library preparation performed and sequenced on the NovaSeq SP 100 (200,000 reads/nucleus) by the Oncogenomics Core Facility at University of Miami Miller School of Medicine.

After sequencing, Illumina output was processed using CellRanger v3.0.2. Base call files for each sample were demultiplexed. A pre-mRNA reference was generated with CellRanger mkref using the mm10 mouse genome. Each sample was aligned to the custom mm10 mouse reference genome using CellRanger. Sample reads were sequenced across two lanes and concatenated after alignment, resulting in a single count matrix per sample.

Pre-processing and quality control—To distinguish nuclei-containing droplets from empty droplets, we performed cell calling on the unfiltered UMI count matrices using a combination of barcode-ranking and the empty-droplet detection emptyDrops function as implemented in the DropletUtils R package.[55] First, nuclei were ranked according to total UMI count and visualized in a log-total UMI vs. log rank plot (Figure S1A). A spline curve was fit to the data to identify "knee" and inflection points, and cells with total UMI count above the knee were considered nuclei-containing droplets. Next, we used the emptyDrops algorithm to further distinguish empty droplets from nuclei for nuclei with lower total UMI counts.

To remove potential doublets, we applied the Python package Scrublet[60] to each individual sample using default parameters. In brief, Scrublet simulates multiplets by sampling from the data and builds a nearest-neighbor-based classifier. Cells with high doublet scores were flagged and removed.

We performed further quality control based on metrics such as total UMI, number of unique genes detected, and mitochondrial transcript content (Figure S1B). Lower-bound thresholds for total UMI and unique gene detection rates were determined by computing three absolute median deviations (MADs) below the median. Across all samples, mean total UMI was 10,556 (E19, 7,457; P4, 9,882; P8, 10,957; P21, 13,928), mean total genes detected was 3,550 (E19, 3,030; P4, 3,574; P8, 3,643; P21, 3,953), and mean mitochondrial transcript content was 0.62% (E19, 0.70%; P4, 0.98%; P8, 0.41%; P21, 0.39%). Remaining high-quality nuclei were used for downstream analysis.

Since donor cells were not tagged prior to pooling, we could not measure the relative cell yield per donor mouse. To approximate the distribution of sexes to cell-types and subtypes, we calculated the percentage of *Xist*+ cells per sample and per cluster. We found that samples E19, P4, P8, and P21 were 0.9%, 46.0%, 40.7%, and 68.1% *Xist*+ cells, respectively, with a mean of 37.7% across all cells from all samples. From this, we speculated that sex-specific gene expression may contribute to batch effects and/or sex-specific clusters. However, we also found that neuron subtypes ranged in *Xist*+ percentage from 15.6% to 51.6% with a mean of 37.5%. This suggests that sex-specific gene expression did not strongly drive neuron subtype clustering results and that our neuron subtype analysis captures gene expression variation irrespective of sex.

Integrated identification of all cell types across development—We first performed standard single-nucleus RNAseq analysis using the Seurat R package (v4.2.1).[61] We observed significant batch effects between samples from each developmental time point; for example, neurons from P21 clustered separately from neurons from all other time points

due to detection of contaminant ambient RNAs such as *Plp1* (Figure S1C). Based on this observation, we determined that Data Integration was necessary.

To better identify shared and unique cell types across all developmental time points, we performed integrated analysis as outlined in Seurat's Data Integration workflow.[62] In brief, after UMI count matrices were log-normalized, the top 2,500 variable genes and first 15 principal components were used for dimensional reduction and clustering. Cell types were identified using a combination of DE testing, comparisons against reference data sets, and prior knowledge of cell type-specific marker genes. For DE testing to identify markers, we used the FindAllMarkers function in Seurat using default parameters. For comparisons against reference data sets, we used the SingleR R package.[35] See methods section on "Comparison of neuronal subtypes to reference data" for description of the SingleR method. After cell type identification, DEGs were recomputed again using the FindAllMarkers function. We principally used the following genes for cell type identification: Excitatory neurons, *Slc17a6*; Inhibitory neurons, *GAD1*; Astrocytes, *Aqp4* and *Gfap*; Oligodendrocyte-lineage cells, *Cspg4, Bmp4, Mbp*; Dividing cells, *Mki67*; Microglia, *P2ry12*; Endothelial cells, *Cldn5*; Vascular Leptomeningeal cells, *Col1a1*; Epithelial cells, *Cdh1*.

Integrated analysis of neurons across development—To investigate neuronal heterogeneity and identify neuronal sub-types, we performed a similar integrated analysis as described above with certain modifications. First, we used the top 3000 variable genes and top 10 principal components for dimensional reduction and clustering. Principal components were determined using the "elbow" plot heuristic. We also set the "resolution" parameter in the FindClusters function to 0.72 based on empirical observations that at this resolution neuron clusters could be identified using single or a small set of genes. Neuronal subtypes were annotated using these parameters. Neuronal subtype marker genes were computed using the FindAllMarkers function and filtered by taking the top 2 genes by p value and then by log(fold-change). To better identify sub-type markers within each of the excitatory and inhibitory neuron classes, we extracted each class and reperformed DE tests via FindAllMarkers. We used the default Seurat log2(fold-change) threshold of 0.25 and adjusted p value threshold of 0.05 for determining the number of DEGs (Figures S2E and S2F). We further quantified the similarity between neuron subtypes by constructing a dendrogram relating the average expression profile of neuron subtypes using the same genes used for cluster analysis (Figure S2D).

We also sought to identify gene expression changes in all excitatory or inhibitory neurons across development using the FindMarkers function. We observed that many of the top DEGs between time points were non-neuronal, e.g., the gene *Ttr*, which has been shown to be specific to cells of the choroid plexus in the CNS.[63] We reasoned that many of these genes may be derived from the ambient RNA during droplet processing.[64] To mitigate the effects of ambient RNA contamination in DE testing, we applied ambient profile estimation algorithms in the DropletUtils R package (Figure S1A). In brief, unfiltered UMI count matrices, containing transcript quantifications for all 10X Chromium lipid encapsulations, were used to estimate the ambient RNA profile based on expression data from low total UMI droplets. We used the ambientContribMaximum function to then filter out genes from DE test results which had an average maximum ambient RNA count contribution greater than

20% across all samples in the comparison. This approach was also applied in identifying gene expression changes across developmental time points for non-neuronal populations.

To further characterize the global changes in neuronal gene expression across development, we combined all neuronal cells into a single group and performed time point comparisons as well as ambient RNA filtering (Figure S3A). We performed Gene Ontology enrichment analysis for Biological Process terms using these DEGs (Figure S3B) using the topGO R package version 2.50.0.

To investigate potential development trajectories between neuronal subtypes, we used the Monocle3 R package.[57] We ported the Seurat dataset into Monocle3 and followed the Monocle3 pipeline except for the following parameters: for preprocess_cds() we “num_dim” to 20 for the PCA; we performed batch correction using align_cds(); we set the root node using the graphical interface prompted by order_cells(). To identify DEGs along trajectories, we used the graph_test() function using default parameters. We clustered DEGs using the find_gene_modules() function and setting the resolution parameter to range from 10^−6 to 10^−1 with increasing exponent.

Comparison of neuronal subtypes to reference data—To compare the neuronal subtypes identified in our study to neuronal subtypes described previously in other reports studying SC neurons, we applied the SingleR algorithm from the SingleR R package. In brief, SingleR first identifies marker genes for each neuron subtype label in the reference data in a pairwise manner. These genes are then used to compute Spearman correlations between the gene expression profiles of cells from the query dataset and cells of the neuron subtypes from the reference dataset. For each query cell, a per-subtype distribution is generated from the correlation values against cells from that neuron subtype label. For that query cell, the per-subtype label is defined as a fixed quantile (default 0.8) of this distribution. The subtype label with the highest score becomes the predicted subtype of the query cell. Heatmaps demonstrating the per-reference-label contribution to each neuronal subtype in the current study were generated using these labels.

To perform an integrated analysis, we pulled data from Cheung et al., Tsai et al., and the current study. For each dataset, we first performed an initial cluster analysis to identify neuronal cells using the marker genes *Slc17a6, GAD1*, and *GAD2* and took the subset of data along genes which were shared among all datasets. We then computed the top variable genes for dimensional reduction using the modeleGeneVar() function from the BioConductor package *scran*.[58] We set the “block” argument to individually sequenced samples as our initial cluster analyses revealed significant batch effects between and within studies. We performed batch correction using the Seurat integration pipeline using default parameters and set the PCA dimensions to 20 for dimensional reductions.

Investigation of adhesion and axon guidance molecules—To perform a comprehensive query of cell adhesion and axon guidance molecules, we pulled gene sets from the following sources: extracellular matrix and adhesion molecules were pulled from GeneCopoeia’s ExProfile Extracellular Matrix and Adhesion Molecules gene panel; axon guidance molecules were pulled from the KEGG pathway database using the pathway ID

"mmu04360". To investigate the heterogeneity of expression of these molecules in SC nuclei, we performed integrated cluster analysis using the Seurat integration pipeline as described above using these gene sets.

Assessment of projections of Pax7-expressing SC neurons—For Cre-dependent anterograde labeling of Pax7 expressing neurons in the superficial SC (sSC), approximately 100 nL of AAV2–CAG–FLEX–GFP (University of North Carolina Vector Core) was injected into the sSC of Pax7-Cre mice (10 weeks old). Injection coordinates were as follows: posterior from bregma, lateral from midline, and depth in mm, 4.16, 0.2, 0.5, and 1.0–1.2, respectively. Three to 4 weeks after AAV injection, mice were anesthetized and then transcardially perfused with 4% paraformaldehyde in phosphate buffered saline (PBS). Brains were dissected and postfixed in 4% paraformaldehyde in PBS for 16 h, and cryoprotected in 30% sucrose in PBS for 2–3 days. Brains were embedded in OCT compound (Tissue-Tek) and coronal sections (20 μm) were cut using a cryostat. Sections were immunostained by incubating in primary antibodies in 5% Normal Goat Serum in PBS with 0.3% Triton X-overnight at 4°C. Primary antibodies used were: RFP (Rockland 600–401-379S, 1:1000) and GFP (Abcam ab13970, 1:2000). Following primary antibody incubation, sections were washed and incubated in species-appropriate Alexa Fluor IgG (H + L) secondary antibodies (Invitrogen, 1:500) at room temperature for 1 h. Slides were mounted using Vectashield with DAPI (Vector Laboratories H-1200). Images were obtained using a Nikon Eclipse Ti fluorescent microscope or an Olympus FluoView 1000 confocal microscope.

Fluorescent *in situ* hybridization (FISH)—RNAscope FISH was performed on 20 μm thickness coronal brain sections from adult mice (8 weeks old) using the RNAscope Multiplex Fluorescent v2 Assay (ACD Biotechne, Catalog No. 323100) according to the manufacture's protocol. Target probes used are listed in the key resources table. TSA-based fluorophores were from PerkinElmer (TSA Plus Fluorescein, PN NEL741001KT; TSA Plus Cyanine 3, PN NEL744001KT; TSA Plus Cyanine 5, NEL745001KT). Images were acquired using an Olympus Confocal FV1000 microscope or an Andor Dragonfly confocal microscope.

Supplementary Material

Refer to Web version on PubMed Central for supplementary material.

ACKNOWLEDGMENTS

This work was supported by grants from the National Eye Institute (NEI) R01EY022961 (K.K.P.), NEI R01EY032542 (K.K.P.), NEI 1U01EY027257 (K.K.P.), NEI R21EY031026 (K.K.P.), DOD W81XWH-19-1-0736 (K.K.P.), The Miami Project to Cure Paralysis and the Buoniconti Fund (K.K.P.), and Glaucoma Research Foundation (K.K.P.). We thank Dr. April Mann for manuscript editing.

REFERENCES

1. Sparks DL, and Mays LE (1990). Signal transformations required for the generation of saccadic eye movements. Annu. Rev. Neurosci 13, 309–336. 10.1146/annurev.ne.13.030190.001521. [PubMed: 2183679]

2. Shang C, Chen Z, Liu A, Li Y, Zhang J, Qu B, Yan F, Zhang Y, Liu W, Liu Z, et al. (2018). Divergent midbrain circuits orchestrate escape and freezing responses to looming stimuli in mice. Nat. Commun 9, 1232. 10.1038/s41467-018-03580-7. [PubMed: 29581428]

3. Wei P, Liu N, Zhang Z, Liu X, Tang Y, He X, Wu B, Zhou Z, Liu Y, Li J, et al. (2015). Processing of visually evoked innate fear by a non-canonical thalamic pathway. Nat. Commun 6, 6756. 10.1038/ncomms7756. [PubMed: 25854147]

4. Shang C, Liu A, Li D, Xie Z, Chen Z, Huang M, Li Y, Wang Y, Shen WL, and Cao P (2019). A subcortical excitatory circuit for sensory-triggered predatory hunting in mice. Nat. Neurosci 22, 909–920. 10.1038/s41593-019-0405-4. [PubMed: 31127260]

5. Zhang Z, Liu WY, Diao YP, Xu W, Zhong YH, Zhang JY, Lazarus M, Liu YY, Qu WM, and Huang ZL (2019). Superior Colliculus GABAergic Neurons Are Essential for Acute Dark Induction of Wakefulness in Mice. Curr. Biol 29, 637–644.e3. 10.1016/j.cub.2018.12.031. [PubMed: 30713103]

6. May PJ (2006). The mammalian superior colliculus: laminar structure and connections. Prog. Brain Res 151, 321–378. 10.1016/S0079-6123(05)51011-2. [PubMed: 16221594]

7. Basso MA, and May PJ (2017). Circuits for Action and Cognition: A View from the Superior Colliculus. Annu. Rev. Vis. Sci 3, 197–226. 10.1146/annurev-vision-102016-061234. [PubMed: 28617660]

8. Benavidez NL, Bienkowski MS, Zhu M, Garcia LH, Fayzullina M, Gao L, Bowman I, Gou L, Khanjani N, Cotter KR, et al. (2021). Organization of the inputs and outputs of the mouse superior colliculus. Nat. Commun 12, 4004. 10.1038/s41467-021-24241-2. [PubMed: 34183678]

9. Ito S, and Feldheim DA (2018). The Mouse Superior Colliculus: An Emerging Model for Studying Circuit Formation and Function. Front. Neural Circ 12, 10. 10.3389/fncir.2018.00010.

10. Cang J, Savier E, Barchini J, and Liu X (2018). Visual Function, Organization, and Development of the Mouse Superior Colliculus. Annu. Rev. Vis. Sci 4, 239–262. 10.1146/annurev-vision-091517-034142. [PubMed: 29852095]

11. Cang J, Wang L, Stryker MP, and Feldheim DA (2008). Roles of ephrin-as and structured activity in the development of functional maps in the superior colliculus. J. Neurosci 28, 11015–11023. 10.1523/JNEUROSCI.2478-08.2008. [PubMed: 18945909]

12. Feldheim DA, and O'Leary DDM (2010). Visual map development: bidirectional signaling, bifunctional guidance molecules, and competition. Cold Spring Harbor Perspect. Biol 2, a001768. 10.1101/cshperspect.a001768.

13. Rashid T, Upton AL, Blentic A, Ciossek T, Knöll B, Thompson ID, and Drescher U (2005). Opposing gradients of ephrin-As and EphA7 in the superior colliculus are essential for topographic mapping in the mammalian visual system. Neuron 47, 57–69. 10.1016/j.neuron.2005.05.030. [PubMed: 15996548]

14. Huberman AD, Feller MB, and Chapman B (2008). Mechanisms underlying development of visual maps and receptive fields. Annu. Rev. Neurosci 31, 479–509. 10.1146/annurev.neuro.31.060407.125533. [PubMed: 18558864]

15. Huberman AD, Manu M, Koch SM, Susman MW, Lutz AB, Ullian EM, Baccus SA, and Barres BA (2008). Architecture and activity-mediated refinement of axonal projections from a mosaic of genetically identified retinal ganglion cells. Neuron 59, 425–438. 10.1016/j.neuron.2008.07.018. [PubMed: 18701068]

16. Kim IJ, Zhang Y, Meister M, and Sanes JR (2010). Laminar restriction of retinal ganglion cell dendrites and axons: subtype-specific developmental patterns revealed with transgenic markers. J. Neurosci 30, 1452–1462. 10.1523/JNEUROSCI.4779-09.2010. [PubMed: 20107072]

17. Martersteck EM, Hirokawa KE, Evarts M, Bernard A, Duan X, Li Y, Ng L, Oh SW, Ouellette B, Royall JJ, et al. (2017). Diverse Central Projection Patterns of Retinal Ganglion Cells. Cell Rep. 18, 2058–2072. 10.1016/j.celrep.2017.01.075. [PubMed: 28228269]

18. Bakken TE, Hodge RD, Miller JA, Yao Z, Nguyen TN, Aevermann B, Barkan E, Bertagnolli D, Casper T, Dee N, et al. (2018). Single-nucleus and single-cell transcriptomes compared in matched cortical cell types. PLoS One 13, e0209648. 10.1371/journal.pone.0209648. [PubMed: 30586455]

19. Velmeshev D, Schirmer L, Jung D, Haeussler M, Perez Y, Mayer S, Bhaduri A, Goyal N, Rowitch DH, and Kriegstein AR (2019). Single-cell genomics identifies cell type-specific molecular changes in autism. Science 364, 685–689. 10.1126/science.aav8130. [PubMed: 31097668]

20. Becht E, Mclnnes L, Healy J, Dutertre CA, Kwok IWH Ng LG, Ginhoux F, and Newell EW (2018). Dimensionality reduction for visualizing single-cell data using UMAP. Nat. Biotechnol 37, 38–44. 10.1038/nbt.4314.
21. Zhang Z, Jiao YY, and Sun QQ (2011). Developmental maturation of excitation and inhibition balance in principal neurons across four layers of somatosensory cortex. Neuroscience 174, 10–25. 10.1016/j.neuroscience.2010.11.045. [PubMed: 21115101]
22. Xie Z, Wang M, Liu Z, Shang C, Zhang C, Sun L, Gu H, Ran G, Pei Q, Ma Q, et al. (2021). Transcriptomic encoding of sensorimotor transformation in the midbrain. Elife 10, e69825. 10.7554/eLife.69825. [PubMed: 34318750]
23. Kalish BT, Cheadle L, Hrvatin S, Nagy MA, Rivera S, Crow M, Gillis J, Kirchner R, and Greenberg ME (2018). Single-cell transcriptomics of the developing lateral geniculate nucleus reveals insights into circuit assembly and refinement. Proc. Natl. Acad. Sci. USA 115, E1051–E1060. 10.1073/pnas.1717871115. [PubMed: 29343640]
24. Byun H, Kwon S, Ahn HJ, Liu H, Forrest D, Demb JB, and Kim IJ (2016). Molecular features distinguish ten neuronal types in the mouse superficial superior colliculus. J. Comp. Neurol 524, 2300–2321. 10.1002/cne.23952. [PubMed: 26713509]
25. Wheatcroft T, Saleem AB, and Solomon SG (2022). Functional Organisation of the Mouse Superior Colliculus. Front. Neural Circ 16, 792959. 10.3389/fncir.2022.792959.
26. Masullo L, Mariotti L, Alexandre N, Freire-Pritchett P, Boulanger J, and Tripodi M (2019). Genetically Defined Functional Modules for Spatial Orienting in the Mouse Superior Colliculus. Curr. Biol 29, 2892–2904.e8. 10.1016/j.cub.2019.07.083. [PubMed: 31474533]
27. Thompson JA, Zembrzycki A, Mansouri A, and Ziman M (2008). Pax7 is requisite for maintenance of a subpopulation of superior collicular neurons and shows a diverging expression pattern to Pax3 during superior collicular development. BMC Dev. Biol 8, 62. 10.1186/1471-213X-8-62. [PubMed: 18513381]
28. Pannasch U, Freche D, Dallérac G, Ghézali G, Escartin C, Ezan P, Cohen-Salmon M, Benchenane K, Abudara V, Dufour A, et al. (2014). Connexin 30 sets synaptic strength by controlling astroglial synapse invasion. Nat. Neurosci 17, 549–558. 10.1038/nn.3662. [PubMed: 24584052]
29. Chung WS, Allen NJ, and Eroglu C (2015). Astrocytes Control Synapse Formation, Function, and Elimination. Cold Spring Harbor Perspect. Biol 7, a020370. 10.1101/cshperspect.a020370.
30. Ittner E, Hartwig AC, Elsesser O, Wüst HM, Fröb F, Wedel M, Schimmel M, Tamm ER, Wegner M, and Sock E (2021). SoxD transcription factor deficiency in Schwann cells delays myelination in the developing peripheral nervous system. Sci. Rep 11, 14044. 10.1038/s41598-021-93437-9. [PubMed: 34234180]
31. Jontes JD (2018). The Cadherin Superfamily in Neural Circuit Assembly. Cold Spring Harbor Perspect. Biol 10, a029306. 10.1101/cshperspect.a029306.
32. Sanes JR, and Zipursky SL (2020). Synaptic Specificity, Recognition Molecules, and Assembly of Neural Circuits. Cell 181, 536–556. 10.1016/j.cell.2020.04.008. [PubMed: 32359437]
33. Tsai NY, Wang F, Toma K, Yin C, Takatoh J, Pai EL, Wu K, Matcham AC, Yin L, Dang EJ, et al. (2022). Trans-Seq maps a selective mammalian retinotectal synapse instructed by Nephronectin. Nat. Neurosci 25, 659–674. 10.1038/s41593-022-01068-8. [PubMed: 35524141]
34. Cheung V, Chung P, Bjorni M, Shvareva VA, Lopez YC, and Feinberg EH (2021). Virally encoded connectivity transgenic overlay RNA sequencing (VECTORseq) defines projection neurons involved in sensorimotor integration. Cell Rep. 37, 110131. 10.1016/j.celrep.2021.110131. [PubMed: 34936877]
35. Aran D, Looney AP, Liu L, Wu E, Fong V, Hsu A, Chak S, Naikawadi RP, Wolters PJ, Abate AR, et al. (2019). Reference-based analysis of lung single-cell sequencing reveals a transitional profibrotic macrophage. Nat. Immunol 20, 163–172. 10.1038/s41590-018-0276-y. [PubMed: 30643263]
36. Illing RB, Vogt DM, and Spatz WB (1990). Parvalbumin in rat superior colliculus. Neurosci. Lett 120, 197–200. 10.1016/0304-3940(90)90037-a. [PubMed: 1963482]
37. Casagrande VA (1994). A third parallel visual pathway to primate area V1. Trends Neurosci. 17, 305–310. 10.1016/0166-2236(94)90065-5. [PubMed: 7524217]

38. Mize RR (1996). Neurochemical microcircuitry underlying visual and oculomotor function in the cat superior colliculus. Prog. Brain Res 112, 35–55. 10.1016/s0079-6123(08)63319-1. [PubMed: 8979819]
39. Hu H, Gan J, and Jonas P (2014). Interneurons. Fast-spiking, parvalbumin(+) GABAergic interneurons: from cellular design to microcircuit function. Science 345, 1255263. 10.1126/science.1255263. [PubMed: 25082707]
40. Villalobos CA, Wu Q, Lee PH, May PJ, and Basso MA (2018). Parvalbumin and GABA Microcircuits in the Mouse Superior Colliculus. Front. Neural Circ 12, 35. 10.3389/fncir.2018.00035.
41. Mize RR, Luo Q, Butler G, Jeon CJ, and Nabors B (1992). The calcium binding proteins parvalbumin and calbindin-D 28K form complementary patterns in the cat superior colliculus. J. Comp. Neurol 320,243–256. 10.1002/cne.903200208. [PubMed: 1619052]
42. Whyland KL, Slusarczyk AS, and Bickford ME (2020). GABAergic cell types in the superficial layers of the mouse superior colliculus. J. Comp. Neurol 528, 308–320. 10.1002/cne.24754. [PubMed: 31396959]
43. Sooksawate T, Yanagawa Y, and Isa T (2012). Cholinergic responses in GABAergic and non-GABAergic neurons in the intermediate gray layer of mouse superior colliculus. Eur. J. Neurosci 36, 2440–2451. 10.1111/j.1460-9568.2012.08169.x. [PubMed: 22712760]
44. Mize RR (1992). The organization of GABAergic neurons in the mammalian superior colliculus. Prog. Brain Res 90, 219–248. 10.1016/s0079-6123(08)63616-x. [PubMed: 1321459]
45. Gale SD, and Murphy GJ (2014). Distinct representation and distribution of visual information by specific cell types in mouse superficial superior colliculus. J. Neurosci 34, 13458–13471. 10.1523/JNEUROSCI.2768-14.2014. [PubMed: 25274823]
46. Behan M, Steinhacker K, Jeffrey-Borger S, and Meredith MA (2002). Chemoarchitecture of GABAergic neurons in the ferret superior colliculus. J. Comp. Neurol 452, 334–359. 10.1002/cne.10378. [PubMed: 12355417]
47. Gale SD, and Murphy GJ (2018). Distinct cell types in the superficial superior colliculus project to the dorsal lateral geniculate and lateral posterior thalamic nuclei. J. Neurophysiol 120, 1286–1292. 10.1152/jn.00248.2018. [PubMed: 29897837]
48. Lee R, Petros TJ, and Mason CA (2008). Zic2 regulates retinal ganglion cell axon avoidance of ephrinB2 through inducing expression of the guidance receptor EphB1. J. Neurosci 28, 5910–5919. 10.1523/JNEUROSCI.0632-08.2008. [PubMed: 18524895]
49. Rivero O, Selten MM, Sich S, Popp S, Bacmeister L, Amendola E, Negwer M, Schubert D, Proft F, Kiser D, et al. (2015). Cadherin-13, a risk gene for ADHD and comorbid disorders, impacts GABAergic function in hippocampus and cognition. Transl. Psychiatry 5, e655. 10.1038/tp.2015.152. [PubMed: 26460479]
50. Eroglu C, and Barres BA (2010). Regulation of synaptic connectivity by glia. Nature 468, 223–231. 10.1038/nature09612. [PubMed: 21068831]
51. Swanson LW, Cowan WM, and Jones EG (1974). An autoradiographic study of the efferent connections of the ventral lateral geniculate nucleus in the albino rat and the cat. J. Comp. Neurol 156, 143–163. 10.1002/cne.901560203. [PubMed: 4425296]
52. Moore RY, Weis R, and Moga MM (2000). Efferent projections of the intergeniculate leaflet and the ventral lateral geniculate nucleus in the rat. J. Comp. Neurol 420, 398–418. 10.1002/(sici)1096-9861(20000508)420:3<398::aid-cne9>3.0.co;2-9. [PubMed: 10754510]
53. Salay LD, and Huberman AD (2021). Divergent outputs of the ventral lateral geniculate nucleus mediate visually evoked defensive behaviors. Cell Rep. 37, 109792. 10.1016/j.celrep.2021.109792. [PubMed: 34610302]
54. Hao Y, Hao S, Andersen-Nissen E, Mauck WM, Zheng S, Butler A, Lee MJ, Wilk AJ, Darby C, Zager M, et al. (2021). Integrated analysis of multimodal single-cell data. Cell 184, 3573–3587.e29. 10.1016/j.cell.2021.04.048. [PubMed: 34062119]
55. Lun ATL, Riesenfeld S, Andrews T, Dao TP, Gomes T, and participants in the 1st Human Cell Atlas, participants in the 1st Human Cell Atlas Jamboree; and Marioni JC (2019). EmptyDrops: distinguishing cells from empty droplets in droplet-based single-cell RNA sequencing data. Genome Biol. 20, 63. 10.1186/s13059-019-1662-y. [PubMed: 30902100]

56. Griffiths JA, Richard AC, Bach K, Lun ATL, and Marioni JC (2018). Detection and removal of barcode swapping in single-cell RNA-seq data. Nat. Commun 9, 2667. 10.1038/s41467-018-05083-x. [PubMed: 29991676]
57. Cao J, Spielmann M, Qiu X, Huang X, Ibrahim DM, Hill AJ, Zhang F, Mundlos S, Christiansen L, Steemers FJ, et al. (2019). The single-cell transcriptional landscape of mammalian organogenesis. Nature 566, 496–502. 10.1038/s41586-019-0969-x. [PubMed: 30787437]
58. Lun ATL, McCarthy DJ, and Marioni JC (2016). A step-by-step workflow for low-level analysis of single-cell RNA-seq data with Bioconductor. F1000Res. 5, 2122. 10.12688/f1000research.9501.2. [PubMed: 27909575]
59. Zheng GXY, Terry JM, Belgrader P, Ryvkin P, Bent ZW, Wilson R, Ziraldo SB, Wheeler TD, McDermott GP, Zhu J, et al. (2017). Massively parallel digital transcriptional profiling of single cells. Nat. Commun 8, 14049. 10.1038/ncomms14049. [PubMed: 28091601]
60. Wolock SL, Lopez R, and Klein AM (2019). Scrublet: Computational Identification of Cell Doublets in Single-Cell Transcriptomic Data. Cell Syst. 8, 281–291.e9. 10.1016/j.cels.2018.11.005. [PubMed: 30954476]
61. Stuart T, Butler A, Hoffman P, Hafemeister C, Papalexi E, Mauck WM 3rd, Hao Y, Stoeckius M, Smibert P, and Satija R (2019). Comprehensive Integration of Single-Cell Data. Cell 177, 1888–1902.e21. 10.1016/j.cell.2019.05.031. [PubMed: 31178118]
62. Butler A, Hoffman P, Smibert P, Papalexi E, and Satija R (2018). Integrating single-cell transcriptomic data across different conditions, technologies, and species. Nat. Biotechnol 36, 411–420. 10.1038/nbt.4096. [PubMed: 29608179]
63. Herbert J, Wilcox JN, Pham KT, Fremeau RT Jr., Zeviani M, Dwork A, Soprano DR, Makover A, Goodman DS, Zimmerman EA, et al. (1986). Transthyretin: a choroid plexus-specific transport protein in human brain. The 1986 S. Weir Mitchell award. Neurology 36, 900–911. 10.1212/wnl.36.7.900. [PubMed: 3714052]
64. Caglayan E, Liu Y, and Konopka G (2022). Neuronal ambient RNA contamination causes misinterpreted and masked cell types in brain single-nuclei datasets. Neuron 110, 4043–4056.e5. 10.1016/j.neuron.2022.09.010. [PubMed: 36240767]

Highlights

- snRNA-seq on superior colliculus (SC) at various ages reveals cell type diversity
- snRNA-seq analysis reveals genes differentially expressed in the SC during development
- Pax7 is a marker for a subset of GABAergic neurons with long-range axon projection
- A web portal for comparing gene expression profiles in the SC cell types across the ages

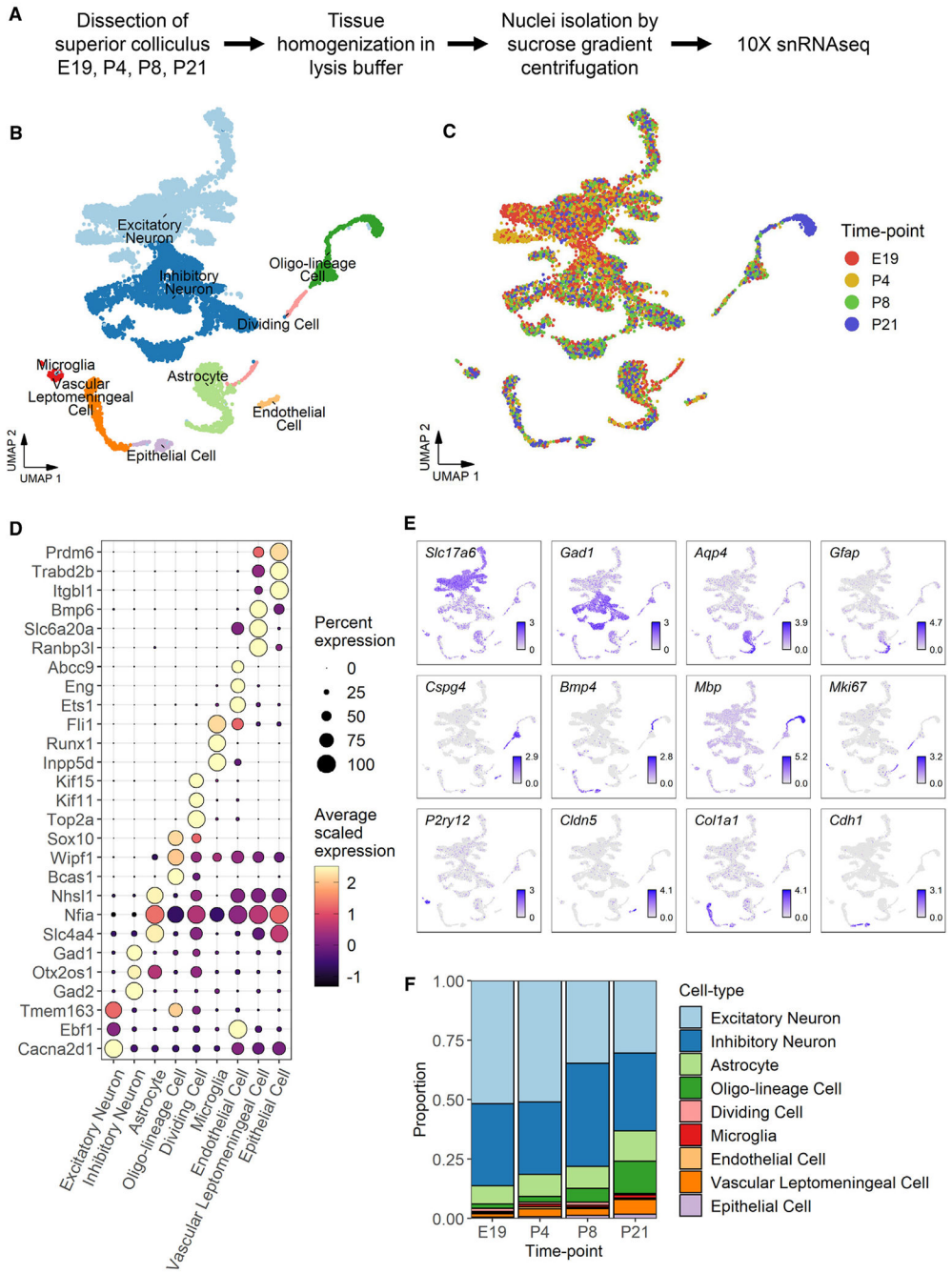

Figure 1. snRNA-seq of developing superior colliculus

(A) Overview of experimental design.

(B) Summary Uniform Manifold Approximation Projection (UMAP) plot of all major cell types identified from integrated analysis. Dots represent gene expression profiles for individual nuclei and are colored by cell type. Size of dots indicates percentage of cells in each group in which a gene is detected. Color of dots indicates the centered and z-scaled log-normalized expression value.

(C) UMAP of nuclei colored by developmental time point of origin.

(D) Dot plot of top three DEGs per cell type.

(E) Marker genes identified previously from the literature used to annotate cell types.

(F) Quantification of cell type proportions across different ages.

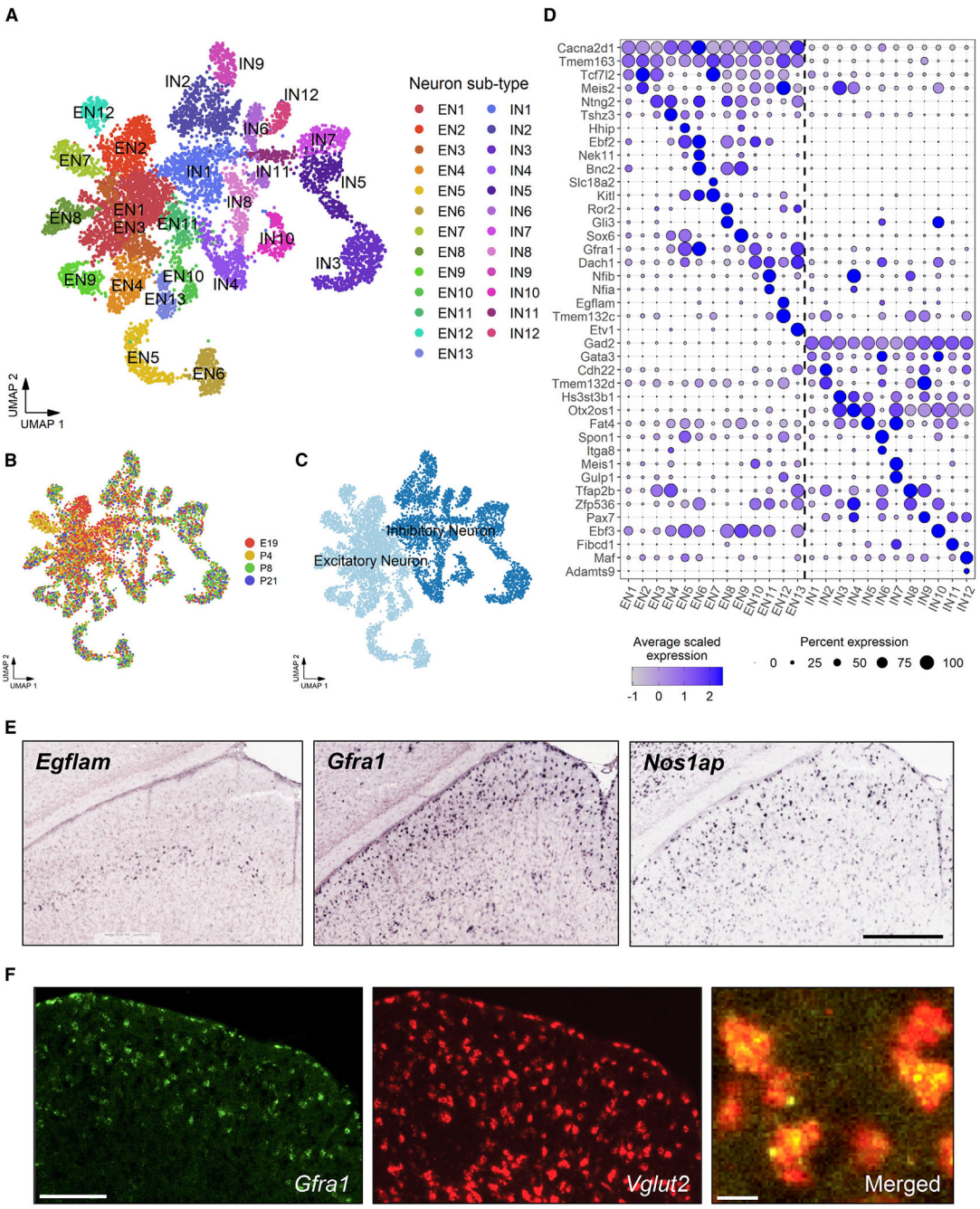

Figure 2. Cluster analysis of neurons reveals transcriptionally and temporally defined neuronal subtypes

(A) UMAP of neuronal subtypes identified through cluster analysis of neuronal cells. Cells are colored by subtype. EN, excitatory neuron subtype; IN, inhibitory neuron subtype.

(B) UMAP of neurons colored by sample developmental time point.

(C) UMAP of neurons colored by principal neuron class.

(D) Dot plot of the top DEGs for each neuronal subtype compared against all other neurons combined. Dashed line partitions excitatory and inhibitory neuronal subtypes. Size of dots

indicates percentage of cells in each group in which a gene is detected. Color of dots indicates the centered and z-scaled log-normalized expression value.

(E) *In situ* hybridization against *Egflam* (left), *Gfra1* (center), and *Nos1ap* (right) from the Allen Brain Atlas. Genes were identified from the list of subtype DEGs as shown in (D) (e.g., *Egflam* and *Gfra1*).

(F) Representative coronal mouse brain sections showing SC. FISH was performed using probes against *Gfra1* (green) and *VGlut2* (red). Scale bars, 500 μm in (E) and (F) (left two panels) and 10 μm (right panel).

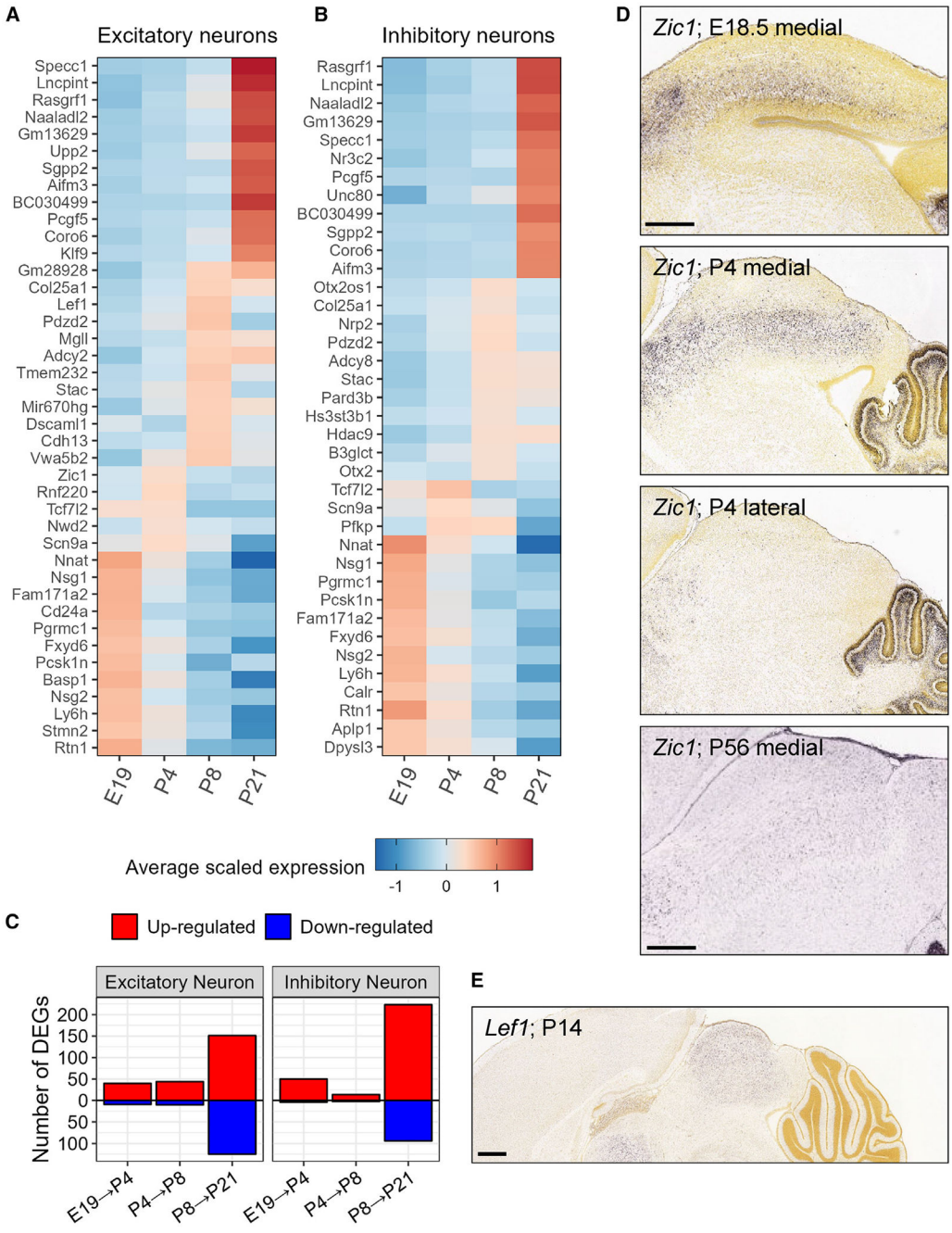

Figure 3. Identification of transcriptional changes across neurons across development

(A and B) Heatmap of the top DEGs per developmental time point in (A) excitatory neurons or (B) inhibitory neurons. Excitatory or inhibitory neuron subtypes were aggregated prior to DE testing.

(C) Quantification of the number of upregulated or downregulated DEGs between sequential developmental time points.

(D) *In situ* hybridization against *Zic1* from the Allen Brain Atlas.

(E) *In situ* hybridization against *Lef1* from the Allen Brain Atlas. Wilcoxon rank-sum test as implemented in Seurat's FindMarkers() function. Scale bars, 500 μm.

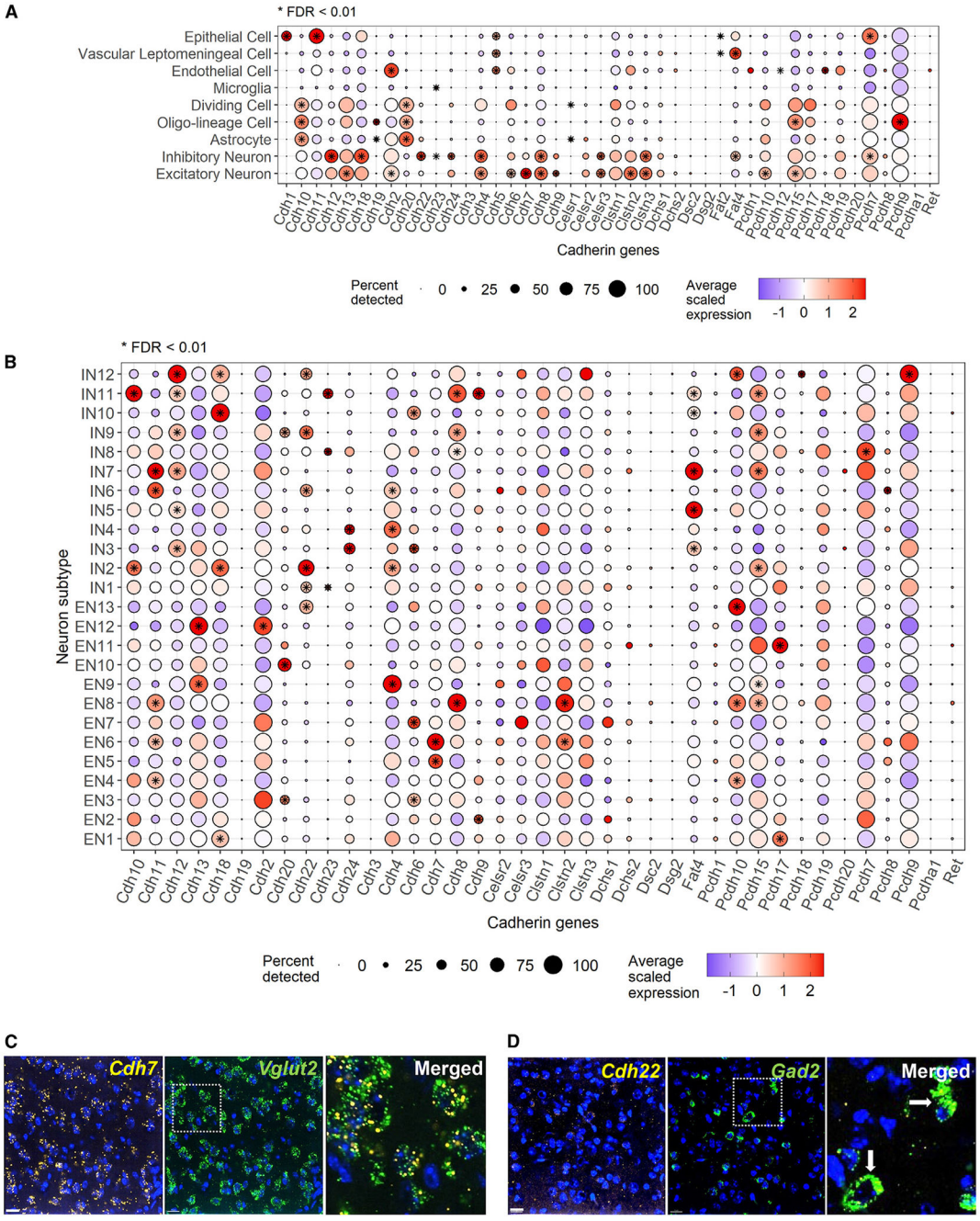

Figure 4. Comprehensive panel of cadherin and protocadherin family gene expression across SC cell types and neuronal subtypes. For all dot plots, size of dots indicates percentage of cells in each group in which a gene is detected. Color of dots indicates the centered and z-scaled log-normalized expression value

(A) Dot plot of scaled gene expression values of cadherin and protocadherin family genes across SC cell types. Only genes that were detected in at least 0.1% of all cells are shown. (B) Dot plot of scaled gene expression values of cadherin and protocadherin family genes across SC neuron subtypes. Only genes that were detected in at least 0.1% of all neuronal cells are shown. Stars indicate statistically significant enrichment of each gene in each group

compared to all other cells combined. Wilcoxon rank-sum test as implemented in Seurat's FindMarkers() function. FDR, false discovery rate.

(C) Two-color FISH against *Cdh7* (yellow) in the SC, a gene enriched in subtypes EN6 and EN7, and excitatory neuron marker *VGlut2* (green). Right panel, higher magnification of the boxed area in the middle panel.

(D) Two-color FISH against *Cdh22* (yellow) in the SC, a gene enriched in several inhibitory neuron subtypes, and inhibitory neuron marker *GAD2* (green). Right panel, higher magnification of the boxed area in the middle panel. Arrows indicate cells that appear to express both *Cdh22* and *GAD2*. Scale bars, 15 μm.

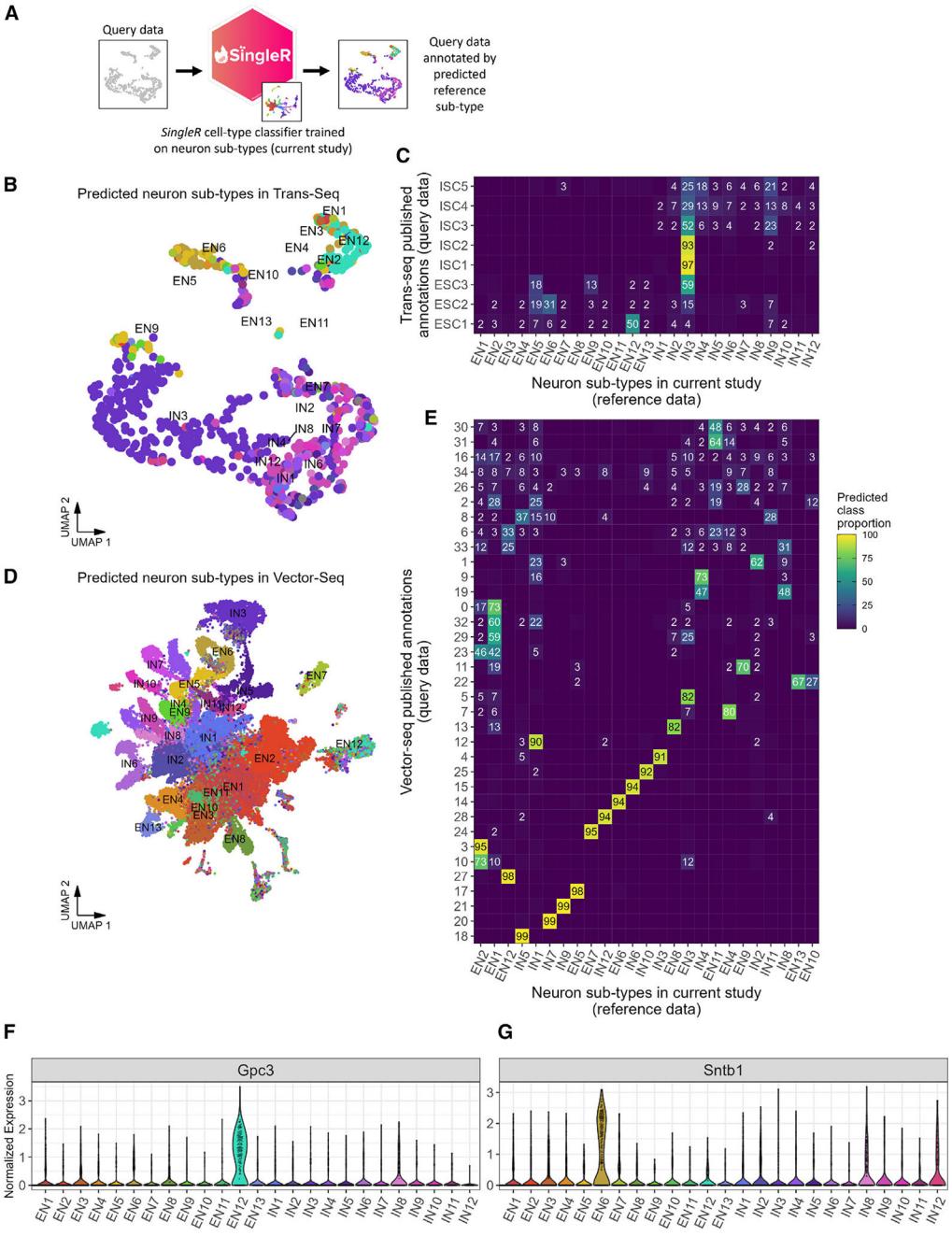

Figure 5. Comparison of neuron subtypes against published SC sn- or scRNA-seq data

(A) Schematic of SingleR approach to classify neurons from published data sources using marker genes of neuron subtypes defined in our analysis. Briefly, for each query cell, SingleR computes correlations between its expression profile and the average expression profile for each reference label (i.e., our subtypes). Query cells in the upper quantiles of per-label correlations are annotated as that label.

(B and D) (B) UMAP of cells from Trans-seq data (see Figure 5B from Tsai et al.[33]) or (D) Vector-seq data (see Figure 3B from Cheung et al.[34]) colored by predicted classification.

(C and E) (C) Heatmap of correspondence between neuron subtypes identified in current analysis and clusters identified by Tsai et al. in Trans-seq, or (E) clusters identified by Cheung et al. in Vector-seq. Heatmap values depict the proportion of cells from y axis clusters that were annotated as x axis neuron subtypes; e.g., 99% of cells in cluster 18 from Vector-seq were classified as IN5 based on marker genes for IN5. Sums along rows equal to 100.

(F and G) Violin plot of *Gpc3* (F) and *Sntb1* (G) expression in excitatory and inhibitory neuron subtype. Clusters Ex-6 (i.e., *Gpc3*+ neurons) and Ex-8 (i.e., *Sntb*$^{+}$ neurons) from Xie et al. correspond to our EN12 and EN6, respectively.

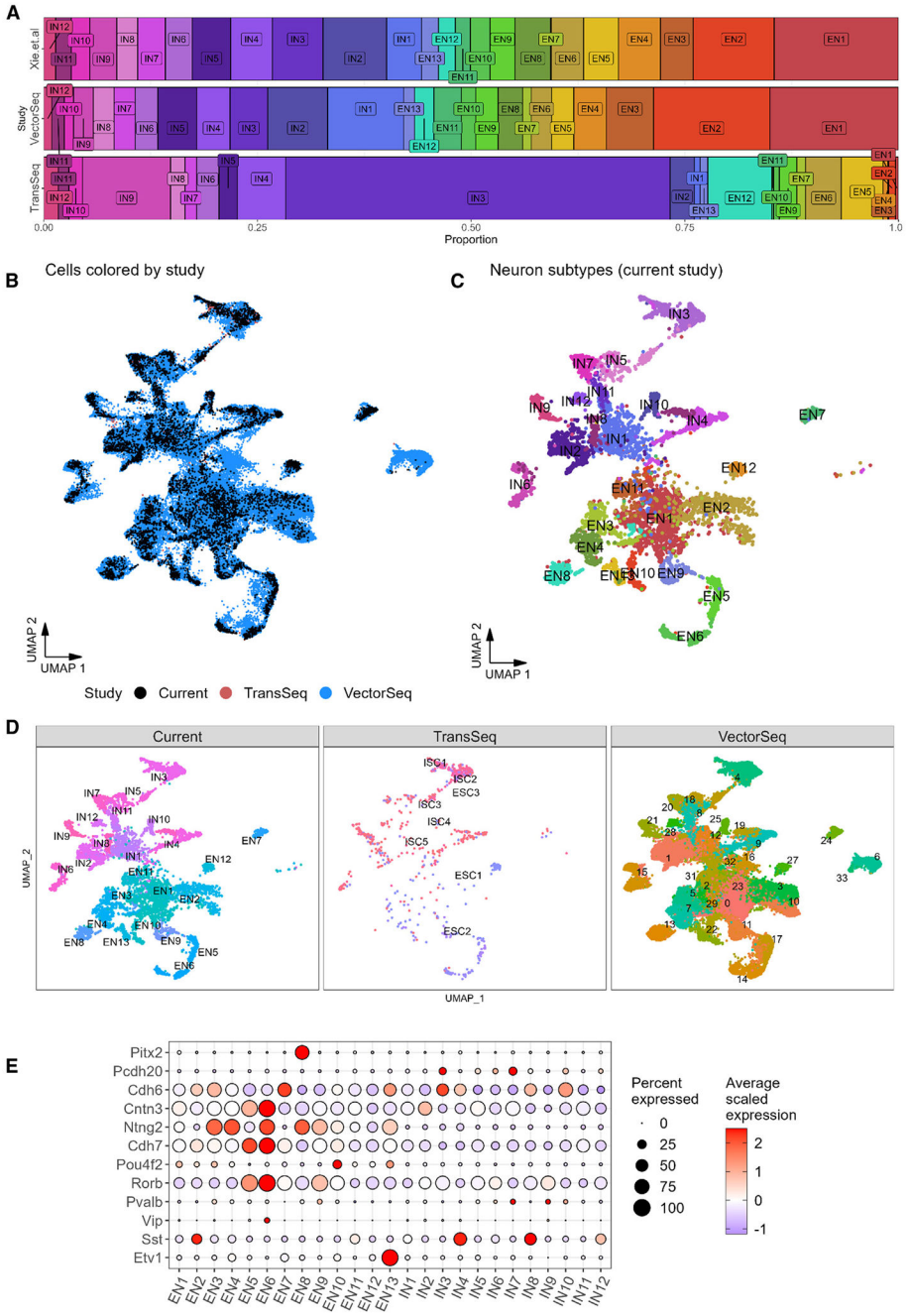

Figure 6. Expression of common SC neuron marker genes and integrated analysis of SC neurons across multiple studies

(A) Stacked bar graph of SingleR neuron subtype predictions across three datasets analyzed. The y axis indicates published studies.

(B) UMAP of SC neurons collected from the current study, the study by Tsai et al. (Trans-seq), and the study by Cheung et al. (Vector-seq). Note the substantial overlap of cells from the current study and cells from Cheung et al.

(C) Same UMAP as (B) except showing only cells from the current study. Cells are colored by neuron subtype.

(D) Same UMAP as (B) except cells are split by study of origin.
(E) Expression dot plot across neuron subtypes of common marker genes identified from previous studies on SC neurons. Size of dots indicates percentage of cells in each group in which a gene is detected. Color of dots indicates the centered and z-scaled log-normalized expression value.

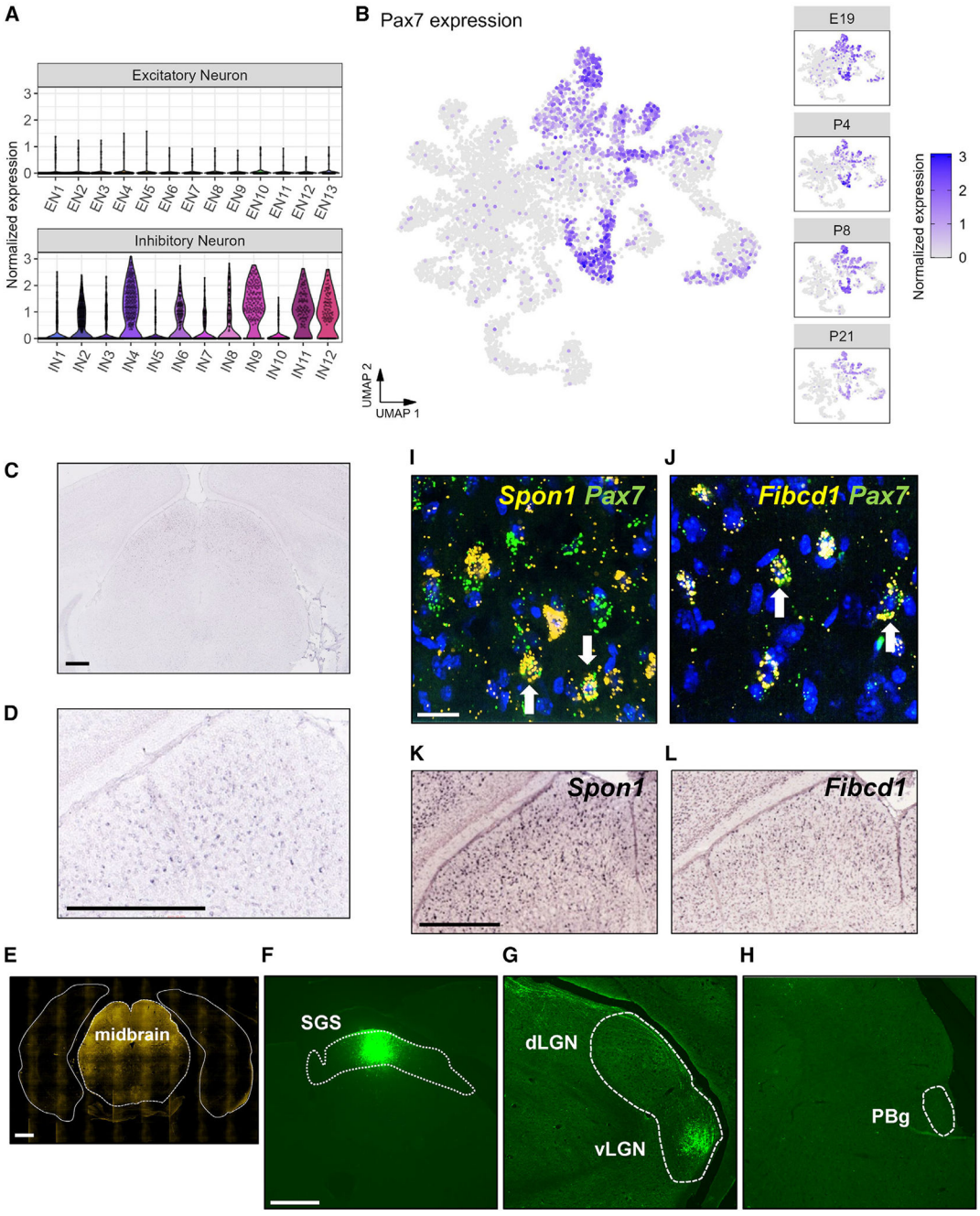

Figure 7. *Pax7*$^{+}$ cells are a population of GABAergic neurons some of which have a common downstream brain target

(A) Violin plot of *Pax7* expression in excitatory and inhibitory neuron subtype demonstrating that detection of *Pax7* is limited to a subset of inhibitory neurons.

(B) Left: UMAP of *Pax7* expression in SC neurons. Right: UMAP of *Pax7* expression in SC neurons across the four developmental time points collected.

(C) *In situ* hybridization against *Pax7* from Allen Brain Atlas. *Pax7* expression is restricted to the midbrain.

(D) Higher magnification of the SC in (C).

(E) tdTomato expression in a coronal section of brain from Pax7-Cre; Rosa26-tdTomato double transgenic mouse. Consistent with the *in situ* hybridization (C), tdTomato expression is restricted to the midbrain.

(F–H) GFP expression in the SC (F), LGN (G), and PBg (H). White dotted areas indicate the respective nuclei.Adult Pax7-Cre; Rosa26-tdTomato received injection of AAV2-FLEX-GFP into the sSC.

(I) Two-color FISH against *Spon1* and *Pax7* in the adult SC. Arrows indicate cells that appear to express both genes.

(J) Two-color FISH against *Fibcd1* and *Pax7* in the adult SC. Arrows indicate cells that appear to express both genes.

(K) ISH image of the SC from Allen Brain Atlas for *Spon1*.

(L) ISH image of the SC from Allen Brain Atlas for *Fibcd1*. Scale bars, 15 μm (I and J). Scale bars, 500 μm (C–H, K, and L).

KEY RESOURCES TABLE

REAGENT or RESOURCE	SOURCE	IDENTIFIER
Antibodies		
Anti-RFP antibody	Rockland	RRID:AB_11182807
Anti-GFP antibody	Abcam	RRID:AB_300798
Bacterial and virus strains		
AAV-FLEX-GFP	University of North Carolina Vector Core	AAV2-CAG-FLEX-GFP
Chemicals, peptides, and recombinant proteins		
TSA Plus Fluorescein	Akoya Biosciences	NEL741001KT
TSA Plus Cyanine 3	Akoya Biosciences	NEL744001KT
TSA Plus Cyanine 5	Akoya Biosciences	NEL745001KT
Critical commercial assays		
Chromium Next GEM Single Cell 3′ Kit v3.1	10X Genomics	1000269
RNAscope® Multiplex Fluorescent v2 Assay	ACD Biotechne	Catalog No. 323100
Deposited data		
Trans-Seq scRNAseq data of SC	Tsai et al.[33]	GEO: GSE202257
Vector-Seq scRNAseq data of SC	Cheung et al.[34]	GEO: GSE189907
snRNAseq data of SC	Xie et al.[22]	GEO: GSE162404
snRNAseq data of SC	This paper	GEO: GSE224407
Experimental models: Organisms/strains		
Pax7-Cre	Jackson Laboratory	010530
Software and algorithms		
Seurat v4	Hao et al.[54]	https://doi.org/10.1016/j.cell.2021.04.048
EmptyDrops	Lun et al.[55]	https://doi.org/10.1186/s13059-019-1662-y
DropletUtils	Griffiths et al.[56]	https://doi.org/10.1038/s41467-018-05083-x
Monocle 3	Cao et al.[57]	https://doi.org/10.1038/s41586-019-0969-x
topGO	R package version 2.52.0.	https://bioconductor.org/packages/release/bioc/html/topGO.html
SingleR	Aran et al.[35]	https://doi.org/10.1038/s41590-018-0276-y

REAGENT or RESOURCE	SOURCE	IDENTIFIER
scran	Lun et al.[58]	https://doi.org/10.12688/f1000research.9501.2
10X Genomics Cell Ranger 3.0.2	Zheng et al.[59]	https://doi.org/10.1038/ncomms14049
Scrublet	Wolock et al.[60]	https://doi.org/10.1016/j.cels.2018.11.005
Analysis Code for this paper	This paper	https://doi.org/10.5281/zenodo.8061024
Other		
RNAscope® Multiplex Fluorescent v2 Assay	ACD Bio.	323100
RNAscope® Probe - Mm-Gfra1	ACD Bio.	431781
RNAscope® Probe -Mm-Slc17a6-C2	ACD Bio.	319171-C2
RNAscope™ Probe- Mm-Cdh7-C2	ACD Bio.	520761-C2
RNAscope™ Probe- Mm-Cdh22-C3	ACD Bio.	573541-C3
RNAscope™ Probe- Mm-Robo3-O1-C2	ACD Bio.	558811-C2
RNAscope™ HiPlex Probe- Mm-Gad2	ACD Bio.	439371
RNAscope™ Probe- Mm-Spon1-C2	ACD Bio.	492671-C2
RNAscope™ Probe- Mm-Fibcd1-C2	ACD Bio.	524021-C2